Journal of the European Ceramic Society 46 (2026) 118127

Contents lists available at ScienceDirect

Journal of the European Ceramic Society

journal homepage: www.elsevier.com/locate/jeurceramsoc

Structure matters: A synchrotron study reveals how crystallite structure influences the deposition mechanism for the powder aerosol deposition method

Daniel Paulus [a], Mario Linz [a,b], Anna-Lena Hansen [c,f], Sander van Smaalen [d], Ralf Moos [a,b,*], Anke Silvia Ulrich [e], Daniela Schönauer-Kamin [a]

[a] Department of Functional Materials, Universitätsstraße 30, 95447 Bayreuth, Germany
[b] Bayerisches Zentrum für Batterietechnik, Weiherstraße 26, 95448 Bayreuth, Germany
[c] Institute for Applied Materials – Energy Storage Systems (IAM-ESS), Karlsruhe Institute of Technology (KIT), Hermann-von-Helmholtz-Platz 1, 76344 Eggenstein-Leopoldshafen, Germany
[d] Laboratory of Crystallography, Bayerisches Geoinstitut, University of Bayreuth, 95447 Bayreuth, Germany
[e] Metals and Alloys II, Prof.-Rüdiger-Bormann-Straße 1, 95447 Bayreuth, Germany
[f] Geschäftsbereich Transfer, Christian-Albrechts-Universität zu Kiel, Christian-Albrechts-Platz 4, 24118 Kiel, Germany

ARTICLE INFO

Keywords:
Aerosol Deposition Method
Deposition Mechanism
Synchrotron XRD
Calcium Cobalt Oxide
Titanium Oxide

ABSTRACT

Powder aerosol deposition (PAD or ADM) is a coating technique to produce ceramic films at room temperature. Although the deposition mechanism has been clarified in some respects, unanswered questions remain. The present work reports films of titanium oxide, which forms a typical PAD microstructure, and films of incommensurate misfit-layered calcium cobalt oxide ($Ca_3Co_4O_{9-\delta}$, CCO-349), which forms a atypical film. For this work, films made of these two materials were examined using X-ray diffraction with synchrotron radiation and a scanning electron microscopy. It turned out that due to its aperiodic crystal structure, CCO-349 can be deformed more easily than conventional technical ceramics like TiO_2. The deformation occurs when the layers in the crystal slide in the direction of the misfit. As a result, it is unnecessary to break the crystals, and a larger crystallite size remains in the film. Therefore, PAD films of CCO-349 have a different microstructure.

1. Introduction

The powder aerosol deposition method, abbreviated ADM or PAD, is a coating process by which ceramic materials can be deposited directly from the powder at room temperature. Kashu et al. were the first to report on this process [1] and Akedo et al. took up the topic a few years later, improved the process and greatly explained the basic deposition mechanism resulting some time later in the Room Temperature Impact Consolidation mechanism (RTIC) [2–4]. Since then, Akedo and his group have made significant contributions to the further development and understanding of PAD [5–10].

Akedo's basic explanation of the deposition mechanism, the RTIC model, can be summarized as follows: During the impact on the substrate, impinging particles break up into fine nanocrystals, which are then hammered into place by subsequent particles (hammering effect) [7]. Plastic deformation also occurs during solidification and hammering. However, a key scientific question is the deposition efficiency of the deposited powder, as after PAD processes residues were found in the deposition chamber. In general, this model still corresponds to how we imagine the deposition mechanism to take place and explains the low deposition efficiency. Recently, our group was able to extend this model. Linz et al. [11] showed that only the outer part of a particle is deposited by using core-shell materials. This explains the low deposition efficiency and helps to understand why a fraction of the powder forms a film while another fraction remains in the deposition chamber, supposedly without having taken part in the process. It, therefore, appears to be the case that a large share of the particles take part in the direct deposition process, but only a small share of each individual particle is deposited. During the initial film formation on the substrate, the substrate is usually roughened, and particles are embedded in the surface. This results in mechanical interlocking of the film and substrate and usually leads to very good film adhesion.

* Corresponding author at: Department of Functional Materials, Universitätsstraße 30, 95447 Bayreuth, Germany.
E-mail addresses: functional.materials@uni-bayreuth.de (D. Paulus), functional.materials@uni-bayreuth.de (R. Moos).

https://doi.org/10.1016/j.jeurceramsoc.2026.118127
Received 17 October 2025; Received in revised form 19 December 2025; Accepted 5 January 2026
Available online 6 January 2026

However, neither Akedo's RTIC model [7] nor the extended RTIC model by Linz et al. [11] that includes the deposition of parts of the particles can explain why some ceramic powders can be deposited with a significantly higher deposition rate than others. These models do also not explain why powder pre-treatment for activation such as grinding, annealing etc. can be essential for successful deposition, which was shown by Exner et al. [12,13]. We therefore propose that the particle morphology may also play a decisive role, as the particle morphology is largely responsible for the force that can be transferred from the impulse of the impinging particle to the small part of the particle that is deposited.

As plastic deformation of the crystals was observed after deposition [7], it is reasonable to assume that the crystal structure of the material to be deposited may have a significant influence. This is because the crystal structure determines how a crystal can deform, how many slip systems it has, how it can break, which kind of defects it can have, and how mobile they are. As with most processes in materials science, the process used to produce a material has a decisive influence on its microstructure. This means that a PAD process modified by a different particle morphology or a different crystal structure will inevitably lead to a different microstructure of the resulting films.

The most frequently investigated ceramics are Al_2O_3, PZT, $BaTiO_3$, and TiO_2 [14]. Tetragonal TiO_2 (space group P42/mnm) is chosen for this study as it shows a very typical deposition behavior. It can be processed with a PAD-typical deposition rate and without a powder pre-treatment to form nanocrystalline films that exhibit a PAD-typical film stress, as the authors were able to show in a previous study [15]. This compressive film stress usually results in a very high hardness of the films.

However, more complex oxides such as calcium cobalt oxide ($Ca_3Co_4O_{9-\delta}$), also called CCO-349, can be deposited with the PAD method, as the authors and other groups have proven [16–18]. All these previous publications show that CCO-349 films have a very unusual microstructure for PAD films. The crystals appear larger than it is usual for PAD. The diffractograms of CCO-349 films show unusually sharp and narrow reflections and also indicate a strong fiber texture. Typical PAD films show a nanocrystalline microstructure, which leads to broad reflections in their X-ray diffraction (XRD) patterns. Although Hasegawa et al. [19] and Furuya et al. [20] have also reported a texture in aluminum oxide films made by the PAD technique, this texture is not nearly as pronounced as that of CCO-349. This is particularly clear in the case of a material with a rather unusual crystal structure, as it is found for the calcium cobalt oxides (CCO). In the composition $Ca_3Co_4O_{9-\delta}$ (CCO-349), this is present in a so-called misfit-layered structure with an oxygen concentration highly depending on the surrounding atmosphere, temperature, and pressure [21,22]. It is precisely this incommensurable structure that gives calcium cobalt oxide poor thermal conductivity with good electrical conductivity, which leads to the superb thermoelectric properties

CCO-349 forms an incommensurate, misfit-layered structure of CoO_2 and Ca_2CoO_3 layers. The incommensurability arises from the mutually incommensurate **b** axes of the two types of layers: $\mathbf{b}_1$ for the CoO_2 subsystem and $\mathbf{b}_2$ for the Ca_2CoO_3 subsystem (Fig. 1). Both subsystems possess monoclinic unit cells with $a_1 = a_2 = 4.83$ Å, $c_1 = c_2 = 10.84$ Å, $\beta_1 = \beta_2 = 98.14°$. and $\alpha_1 = \alpha_2 = \gamma_1 = \gamma_2 = 90°$. The incommensurate composite character of the compound is governed by the **b** lattice parameters, with $\mathbf{b}_1 = 2.82$ Å for the CoO_2 subsystem and $\mathbf{b}_2 = 4.56$ Å for the Ca_2CoO_3 subsystem. This results in a ratio $\mathbf{b}_1/\mathbf{b}_2$ of $\approx 0.6915(1)$. [23] The ratio is an irrational number. This means that a proper supercell does not exist and the superspace approach with two subsystems is required [23].

Calcium cobalt oxide is a promising candidate for an application in thermoelectric energy harvesting because of its unusual crystal structure [24]. Due to the incommensurate composite type of crystal structure and the associated high phonon scattering, CCO-349 has a comparatively low thermal conductivity [25]. At the same time, it has a relatively high electrical conductivity in the basal plane. Orthogonally, however, the electrical conductivity is a decade lower [26], which, in the case of an application, requires the production of a textured material. The anisotropy in the electrical conductivity is due to the conductivity mechanism of CCO-349. While cobalt is predominantly present in oxidation state -III/-IV in the CoO_2 subsystem, oxidation states -II predominate in the Ca_2CoO_3 subsystem. This increases the electron density in the Ca_2CoO_3 subsystem, while electron vacancies are generated in the CoO_2 subsystem. These defect electrons result in the higher in-plane p-type conductivity [24].

Here, we report on the mechanism of deposition of CCO-349 films produced by the PAD technique in comparison to rutile TiO_2 that forms typical PAD-produced films. X-ray diffraction is essential for investigating the influence of the crystal structure on the mechanism of

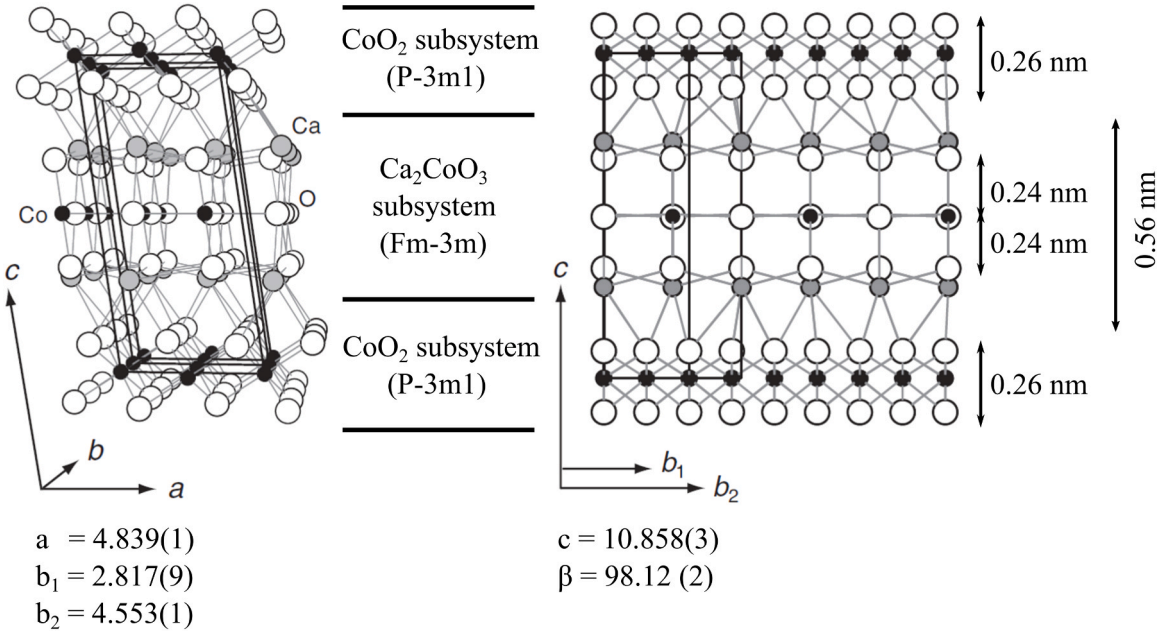

Fig. 1. Crystal structure of calcium cobalt oxide. Reproduced with permission after [23] ©(2002), The Physical Society of Japan.

deposition. However, standard laboratory devices are not suitable for these experiments. Evaluation of this data provides small crystallite sizes and the associated strong reflection broadening, as well as the strong strain broadening as it is typical for aerosol deposited films, lead to very low intensities and correspondingly long measurement times. In addition, films of PAD-CCO-349 only show the (0 0 *l*) reflections during measurements in the Bragg-Brentano setup due to the strong fiber texture [17]. XRD was therefore conducted using synchrotron radiation and a Debye-Scherrer-like setup.

To address these problems, we report X-ray powder diffraction data obtained in a Debye-Scherrer-like setup at the hard x-ray beamline P02.1 [27] of the synchrotron PETRA-III at DESY in Hamburg. The evaluation of this data provides a deep insight into the microstructure of PAD-produced films and their behavior during thermal post-treatment. Furthermore, it provides information on the mechanism of deposition of materials with different crystal structures.

Post-deposition heat treatments up to 1200 °C are widely used to achieve a stable and compact ceramic film. In the case of electrically conductive materials the annealing causes a reduction in microstrain in the film accompanied by a significant increase in electrical conductivity [28]. Films produced with PAD exhibit a compressive stress that relaxes at relatively low temperatures such as around 300 °C. This has also been reported several times [29–31]. The authors have already investigated this relaxation behavior in a previous study [15]. In this study, temperatures from 300 to 800 °C are used and their effect on the film morphology is investigated. This temperature of 300 °C was selected to see the relaxation of the intrinsic compressive stress after heat treatment, at which no change in microstrain and crystallite size should occur [15]. After heat treatment at 600 °C, the microstrain should be largely relaxed without a significant change in crystallite size. At 800 °C, the relaxation of the microstrain should be completed.

2. Experimental

2.1. Powder synthesis and preparation

Starting materials for application of the PAD technique are microcrystalline powders of titanium oxide (TiO_2, rutile structure) and calcium cobalt oxide $Ca_3Co_4O_{9-\delta}$. Commercial TiO_2 powder (99.5 % Rutile phase) was obtained from Alfa Aesar, Haverhill, MA, USA with a particle size of 1.0–2.0 μm and calcium cobalt oxide powder was synthesized by solid-state reaction of cobalt oxide (99.97 %, ChemPUR, Karlsruhe, Germany) and calcium carbonate (99 %, low-alkali, Riedel-de Haën, Seelze, Germany). A stoichiometric mixture of the two starting materials was homogenized in a planetary ball mill (Pulverisette 5, Fritsch GmbH, Idar-Oberstein, Germany), and then calcined in an aluminum oxide crucible at 900 °C for 12 h. After calcination, the powder was ground in the planetary ball mill in a YSZ crucible with YSZ grinding balls. The powders were deagglomerated using a 90 μm sieve and then stored in a drying oven at 200 °C until the film deposition. The particle size distribution of the two starting powders was measured with a Mastersizer 2000 (Instruments Ltd, Malvern, United Kingdom).

2.2. Film preparation by the powder aerosol deposition method and heat treatment

Thin films of CCO-349 and TiO_2 were deposited on 1 mm thick soda-lime glass substrates (New Erie Scientific LLC, Portsmouth, USA) using a custom-built PAD device, see [14]. A convergent slit nozzle with oxygen as the carrier gas was used for spraying. TiO_2 was deposited as films of 10 μm thickness. For CCO-349, the glass substrate had to be roughened with a laser before deposition, as otherwise, the film would have detached from the substrate at the target film thickness of 40 μm as shown by pre-experiments. Three batches of 48 soda-lime substrates with titanium oxide coating and 14 batches of 12 substrates with CCO-349 coatings were produced. Prior to coating, the glass substrates had been scribed with a laser so that they could be split into 4 mm× 4 mm individual samples after coating. An overview of the samples and the treatment conditions that were investigated in this study is given in Table 1.

2.3. Sample characterization

2.3.1. X-ray diffraction

X-ray diffraction was performed at the beamline P02.1 of PETRA III at the German Electron Synchrotron DESY in Hamburg [27]. A Debye-Scherrer-like setup was used. The coated samples were glued onto Kapton foil with Kapton tape and fixed in a high-throughput sample holder for the transmission geometry of beamline P02.1. This is shown in Fig. 2. About 60 samples were measured in one batch with this sample holder. Before the samples, the standards LaB_6 NIST 660c, Si NIST 640b, ZnO NIST 1979 A and B were measured in each batch to determine the instrumental parameters. In addition, the starting powders were characterized during an additional beam time. A Si NIST 640 g standard was used to determine the reflex shape and position during this measurement time. The standard and the samples in powder form were characterized in the same setup as the film samples. The powders were placed in a sealed Kapton bag in the sample holder. One sample of CCO-346 and one sample of TiO_2 were characterized.

A Varex XRD 4343CT detector (150 × 150 μm^2 pixel size, 2880 ×2880 pixel area) was placed 2 m behind the sample holder. The measurements were carried out with a radiation wavelength of 0.20736 Å, which corresponds to a photon energy of approx. 60 keV.

The 2D diffraction images obtained were then integrated into 1D diffractograms using the program DAWN. [32]

2.3.2. Scanning electron microscopy

After XRD, one sample of each type listed in Table 1 was fractured and investigated using scanning electron microscopy (SEM, LEO 1530, Carl Zeiss, Oberkochen, Germany). In addition, the powder was investigated using SEM before deposition. Secondary electron (SE) images of the fracture surface were taken using magnifications in the range of 1000x–25000x and an accelerating voltage of 3 keV. The sample surfaces were previously sputtered with platinum to make it conductive.

2.4. Rietveld refinement

The software TOPAS Academic 64 V7.24 (Cuhelo Software, Brisbane, Australia) was used for Rietveld Refinement. The device-intrinsic reflex broadening was determined using that of LaB_6 NIST 660c or Si NIST 640 g, respectively, and its reflex shape was stored as Thompson-Cox-Hastings peak shape [33]. The background was created as a Chebyshev polynomial. One measurement of each sample type was individually refined to obtain good starting values. A sequential refinement was then carried out with the remaining measurements of this type. Within this sequential refinement, a simulated annealing was performed for each measurement and the fit was allowed to converge 10000 times with slightly different values. Of the parameters obtained, the one with the lowest χ^2 was saved (least square including restraints). The input files used (.INP files) are available in the SI.

Table 1
Overview of investigated samples.

Sample type	Deposited films	Number of 4 mm× 4 mm samples
as-deposited	TiO_2	61
	CCO-349	55
1 h at 300 °C	TiO_2	52
	CCO-349	56
1 h at 600 °C	TiO_2	54
	CCO-349	56
1 h at 800 °C	CCO-349	2

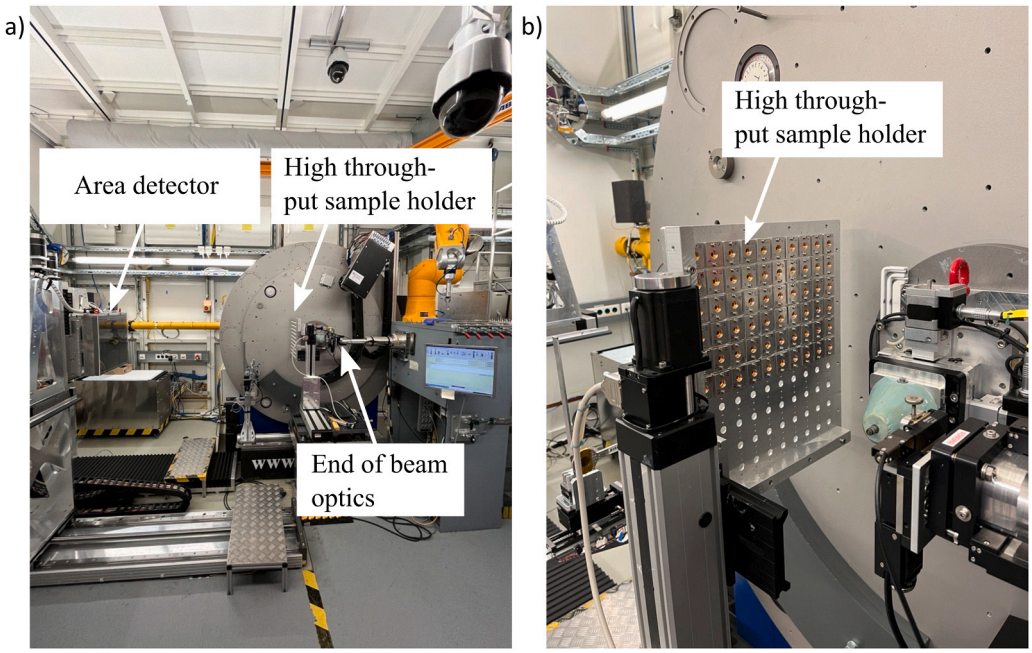

Fig. 2. Photographs of the high throughput setup at beamline P02.1.

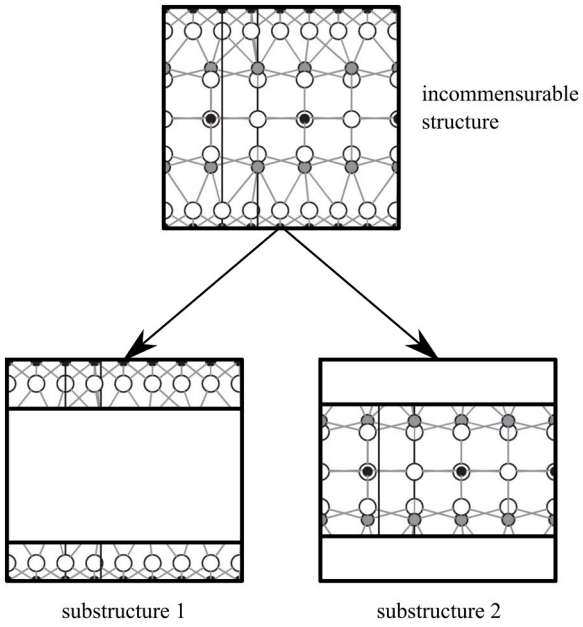

Fig. 3. Schematic sketch of the splitting of the incommensurable superstructure into two substructures. Reproduced with permission [23] ©(2002), The Physical Society of Japan.

2.4.1. Structure refinement of TiO_2

In the case of titanium oxide, in addition to the fundamentally necessary parameters such as "Zero_Error" and the scaling factor, the lattice parameters *a* and *c* were refined. Moreover, crystallite size and microstrain were refined using the double Voight approach according to Balzar et al. [34,35]. The TOPAS macro for preferred orientation, according to March-Dollase [36], was used to simulate a film texture as described by Hasegawa et al. [19].

To stabilize the parameters across the sequential refinement, constraints were set for the lattice parameters *a* and *c* to keep them between 4.50 Å and 4.46 Å and between 2.90 Å and 3.0 Å, respectively. Furthermore, restraints were set to keep the lattice parameters close to the lattice parameters of 4.593635 Å and 2.954969 Å given in the PDF 04–003–0648. Further details on the refinement of the titania measurements can be found in the supplementary information.

2.4.2. Structure refinement of calcium cobalt oxide

The superspace group X2/*m*(0 b 0) s0 [22] of $Ca_3Co_4O_{9-\delta}$ cannot be stored in TOPAS, but can be stored in JANA2020 [37], for example. With JANA2020, however, the microstructure cannot be elucidated nearly as well as with TOPAS. Therefore, a refinement with TOPAS was implemented and a workaround by creating two structures of the space group *Cm*. To make this a reliable model, some parameters of these two structures had to be linked together. The cell parameters *a_global, b1, b2, c1, c2, β1, β2, α_global* and *γ_global* were defined as global parameters. The angles *α_global* and *γ_global* were set globally to 90° and were not refined, but used as cell angles in both subsystem unit cells. The parameter *a_global* was used in both subsystem cells as cell parameter *a*. The parameters *b1* and *b2* were used as individual lattice parameters for the subsystem cells in the misfit direction and not linked, because we want to give the misfit the opportunity to change slightly

In *c*-direction, the reciprocal lattice vector * must be equal for both substructures. Due to the definition of the reciprocal lattice vector, this means that the distance between the layers must remain the same. In other words, the condition in Eq. 1 must be fulfilled.

$$c1\sin\beta1 = c2\sin\beta2 \quad (1)$$

Since such a condition cannot be implemented as a constraint in TOPAS due to the algorithm, the condition was implemented as a very hard restraint, which allows a deviation of the reciprocal lattice vector by a maximum of 10^{-6}, i.e. about 10^{-5} Å, which is below the resolution limit of the XRD set-up.

Since both substructures are part of the same crystals, the crystallite size of the two structures also had to be linked. Therefore, a global value for the Gaussian component and a global value for the Lorentz component of the crystallite size were defined. The parameters for the microstrain were also set globally for both subsystem cells.

The last linking of parameters that needs to be made is the linking of the texture. However, modeling the preferred orientation of PAD CCO-349 films is a challenge due to the strong fiber texture. Since a highly textured material behaves similarly to a powder sample, which exhibits

a preferred orientation of the crystals due to its platelet-shaped particle geometry, the correction functions developed for this purpose can be transferred to the sample with fiber texture.

Several attempts with the March-Dollase model did not lead to a satisfactory result. Therefore, the model of symmetrized harmonics according to Järvinen [38], which is called in TOPAS with the keyword "PO_Spherical_Harmonics", was used to model the preferred orientation. The complex preferred orientation of the CCO-349 films could be satisfactorily modeled with spherical harmonics of up to the order of eight. The parameters used for this had to be defined globally again and applied to both subsystems together in order to model the same preferred orientation in both subsystems.

In the sequential refinement, the fundamentally necessary parameters, such as the scaling factors and the background, were refined. In addition, the five linked lattice parameters, the two size parameters, the two strain parameters, the atomic positions in the cell, and the preferred orientation were refined. Further details and the input files used can be found in the supplementary information. The parameters for the first and independent refinement were taken from PDF 04–016–0860, which is referred to Mugerra et al. [39] 200 was used as the starting value for the crystallite size parameters and 10^{-5} was used for the two microstrain parameters.

2.4.3. Analysis of the refined structures

The crystallite sizes L_{vol}-IB of the samples derived from the reflection broadening for the different sample types were determined from the films XRD patterns after background subtraction. The crystallite size parameter L_{vol}-IB is the third root of the crystallite volume, determined by the size broadening. The "IB" means, that the broadening of the reflections was determined by comparing the integral breadth of the reflections.

3. Results

3.1. Powder properties

The particle size distribution is crucial for successful deposition using PAD. If the particles are too small, they are deflected by the bow shock in the carrier gas before they reach the substrate. If the particles are too large, they create large craters in the surface or cause abrasion of the substrate or the already deposited layer. Fig. 4 shows the particle size distribution curves of the TiO_2 powder and the synthesized CCO-349 powder, determined by laser diffraction.

Both powders have a monomodal particle size distribution. With a d_{50} of 1.075 µm and a narrow logarithmic normal distribution of the particle size, the TiO_2 powder is in a size range that is usually used in PAD [14]. The self-synthesized CCO-349 powder is relatively coarse for a PAD powder with a d_{50} of 8.892 µm. The particle size distribution of the CCO-349 powder is also wider than that of the TiO_2 powder.

SEM images of the titanium oxide powder are shown in Fig. 5 to investigate the powders morphology.

In line with the particle size distribution (Fig. 4), the exemplary particle shown in Fig. 5a) is in the size range 1 µm to 2 µm. It is polycrystalline and consists of weakly bonded primary crystals. The weak connection resembles a sinter neck as it is formed in the early sintering stage. The primary crystals do not resemble the habitus of a tetragonal crystal, but are roundish and have areas on the surface that look as if there had been a neighboring primary crystal at this point, but it has broken off. The size of the primary crystals ranges from 200 nm to 500 nm.

SEM images of CCO-349 particles are shown in Fig. 6. The overview image in Fig. 6a) shows that the particles and the primary crystals are larger than those of the TiO_2 particles.

In contrast to titanium oxide, a kind of habitus is definitely recognizable in CCO. In particular, the platelet-like structure of the large primary crystals matches the misfit-layered structure of the CCO

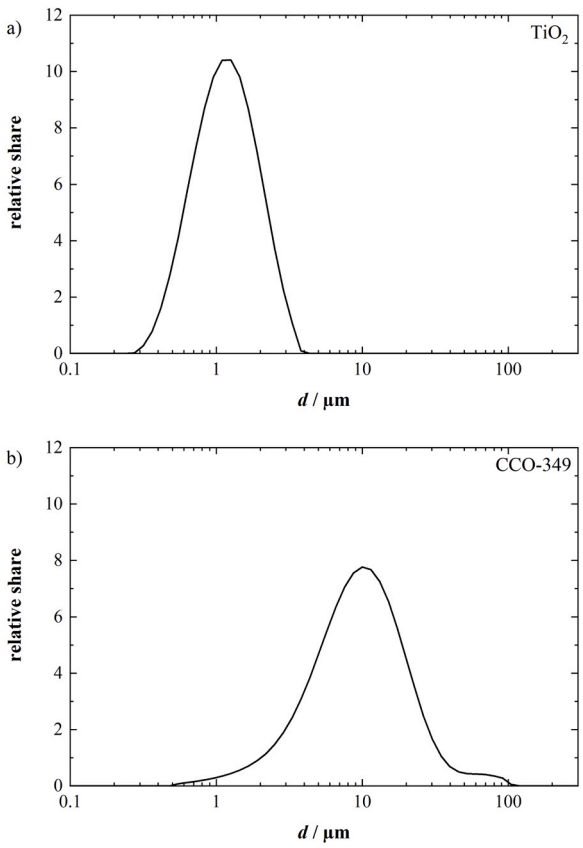

Fig. 4. Particle size distribution of the TiO_2 powder (a) and the CCO-349 powder (b) used to produce the films.

crystals. It is also striking that the layer-like structure is recognizable on the sides of the platelets. However, it is not possible to determine from the SEM images whether this relief-like structure on the edge was caused by sliding on the basal plane during the grinding process or by stacking faults. In addition to these large primary crystals, there are also smaller crystals on the surface in the < 100 nm range.

Some CCO-349 particles also showed an interesting detail. By compressing one corner, the individual layers were displaced against each other and cracks also grew along the layers. This is shown in Fig. 7.

3.2. SEM investigation of the films

Fig. 8 shows overview images of the as-deposited PAD films. They show exemplified how the coatings appear in low magnifications.

The fracture surfaces of the TiO_2 PAD films examined using SEM imaging are shown in Fig. 9 including images after all post-treatments. Their structure and surface topology is similar to that of fracture surfaces usually seen in PAD films [14,29] (Fig. 9-a). Regardless of the heat treatment temperature, fine-grained structures are present that are significantly smaller than 100 nm. Individual larger crystals are not recognizable, nor are pores or cracks. The fracture surfaces confirm that we have produced a typical PAD film, here.

In contrast to the titanium oxide PAD films, the CCO-349 films show a completely different fracture pattern that is atypical for PAD films. The fracture patterns of all sample types listed in Table 1 are shown in Fig. 10. On the fracture images of the CCO-349 films, layer-like structures with a width of 500 nm and more are recognizable. They are often parallel to the substrate plane and stretched perpendicular to the deposition direction. They become larger with increasing heat treatment temperature.

We identify these structures as single crystals of CCO-349. Such large crystals are very unusual for PAD films. Also, the orientation of these

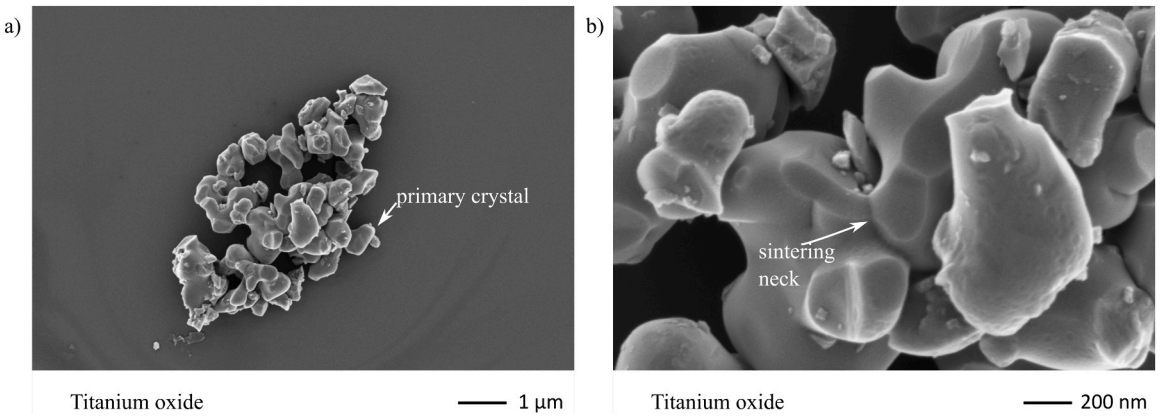

Fig. 5. SEM overview (a) and detailed view (b) of a TiO_2 particle as used as starting powder.

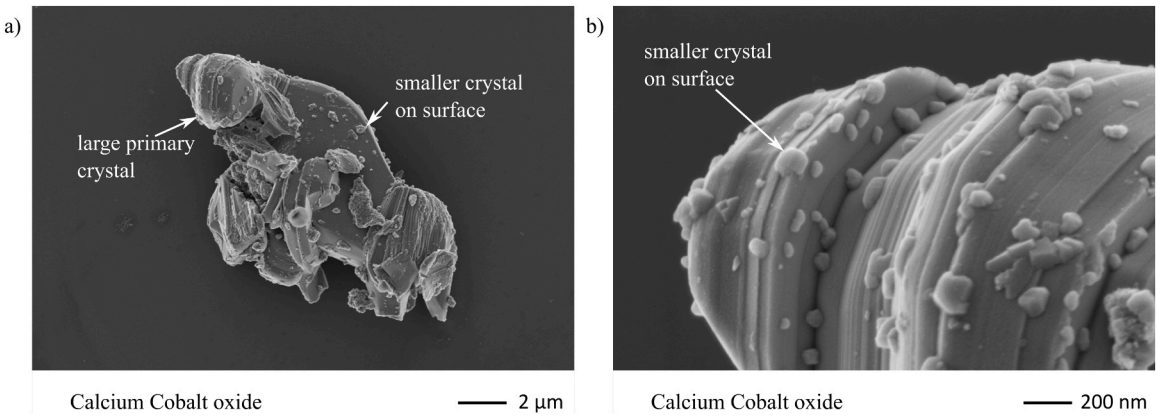

Fig. 6. SEM overview (a) and detailed view (b) of a CCO-349 particle as used to produce the PAD films.

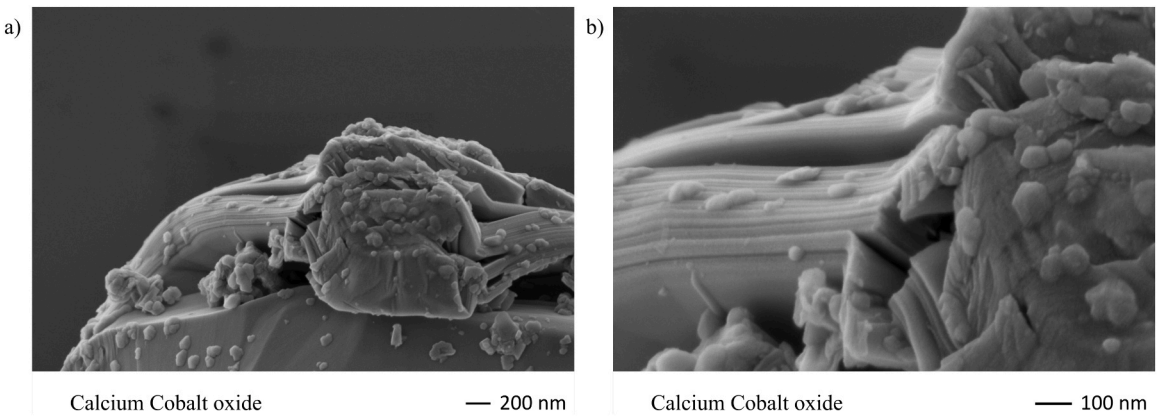

Fig. 7. SEM overview (a) and detailed view (b) recording of a CCO-349 Particles with compressed corner.

platelet-like crystals parallel to the substrate plane is very unusual for PAD films but has already been previously reported in [17]. The SEM of CCO-349 indicated a strong fiber texture, which is in good agreement with previous studies. [16–18]

3.3. Results of XRD

3.3.1. Titanium oxide

The diffraction image of TiO_2 (Fig. 11-a)) shows several narrow and one wider concentric circle. With the exception of the innermost circle, the narrow concentric circles represent the reflections of the TiO_2 PAD film. The innermost narrow circle is a reflection of polyimide (Kapton-foil) used as a carrier material. The wide white ring is caused by diffuse scattering in the amorphous soda-lime glass substrate.

It is noteworthy that the concentric circles are very homogeneous in their gray scale. With a radiographed area of 1 mm× 0.5 mm and a film thickness of approx. 10 µm, the measurement volume is very small. The homogeneous gray scale indicates that there are a sufficient number of crystals in the measured volume, which are also very uniformly oriented in-plane, to ensure such a homogeneous exposure of the detector. The fact that the crystals are concentric circles and not ellipses also indicates that the intrinsic compressive stress in-plane in the film is homogeneous.

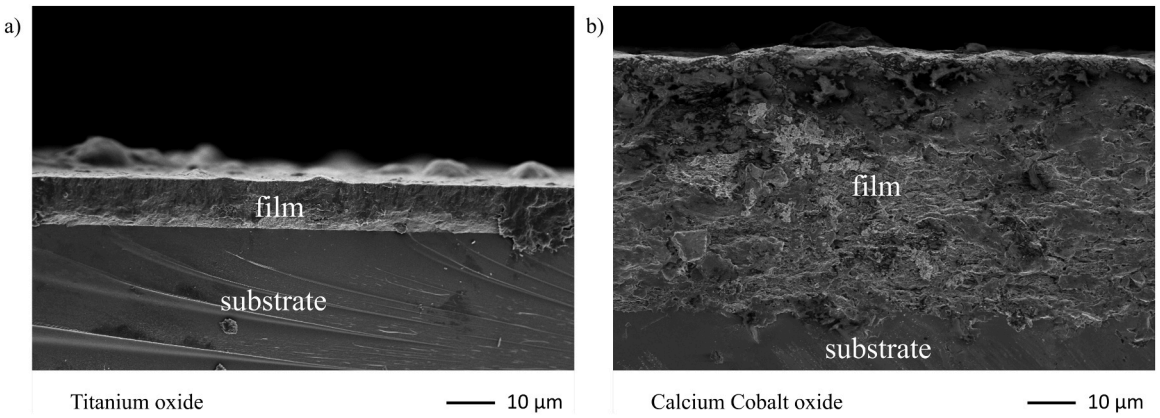

Fig. 8. SEM overview recordings of TiO_2 (a) and CCO-349 (b) fractures of the as-deposited PAD films.

An integrated diffraction pattern of an as-deposited TiO_2 PAD-film is shown as Fig. 11-b). The reflex of polyimide at 0.76° and the broad reflex of glass in the range from 2° to 5° are clearly visible. In addition, the curve fitted using the Rietveld Refinement is shown in red, as well as the corresponding background polynomial (blue) and the difference between the measured and calculated data (orange).

To make it easier to recognize the individual reflections and their assignment to the *hkls*, Fig. 12 shows a measured (black) and the corresponding calculated (red) diffractogram of the measured TiO_2 film after subtraction of the background. The strongly broadened reflexes due to size broadening and microstrain are very typical for PAD films.

The crystallite sizes L_{vol}-IB of the samples derived from the reflection broadening for the different sample types are listed in Table 2. In the as-deposited state, it is approx. 19 nm. The samples that were post-treated at 300 °C or 600 °C have a crystallite size of approx. 14 nm. These crystallite sizes match the value ranges of five to 30 nm typically found in the literature for PAD films [4,13,15,40–46]. The crystallite size of the starting powder was determined to be 300 nm. The strong reduction in particle size typical of PAD has therefore taken place during the deposition. In addition, the crystallite size of the starting powder is therefore in a very favorable range for PAD.

No significant increase in crystallite size is found as a result of the heat treatment. This means that even after 12 h heat treatment at 600 °C grain growth can be neglected. The situation is different with microstrain. The values determined are listed in Table 2.

In the as-deposited state, the films have a microstrain of 0.0170. This is consistent with the values that Yang et al. [46] recently determined for Al_2O_3 on Si substrates. The microstrain is almost halved to 0.0089 when heat treated at 300 °C for 12 h. If heat treated at 600 °C instead of 300 °C, the microstrain is as low as 0.0048. This means that the microstrain of the films treated at 600 °C is still a decade higher than the microstrain of the starting powder.

In addition to the crystallite size and the microstrain, the lattice parameters were refined. The calculated values can be found in Table 3.

Films produced by PAD also exhibit a compressive stress that relaxes at relatively low temperatures. This has also been reported several times in the literature [29–31]. The authors have already investigated this relaxation behavior in a previous study [15]. At that time, the stress was determined using a modified Stoney equation [47,48]. Using the lattice parameters shown in Tables 3 and 4, the compressive residual stress in the PAD-films can be calculated with the following approach.

The residual stress is calculated under the assumption that the Young's modulus behaves linearly with stress and is 267.3 GPa [49]. We now assume that the films are free of compressive stress after heat treatment at 600 °C and use the lattice parameter of the samples annealed at 600 °C and that of the untreated samples to calculate an elongation according to Eq. 2. Various studies have shown that this assumption can be made. [15,29,30] This is also supported by the fact that the lattice parameters of the powder largely match those of the coatings after heat treatment. The parameter ε expresses the dimensionless strain, and the parameter lp is one of the two lattice parameters a or c.

$$\varepsilon = \frac{lp_{RT} - lp_{600°C}}{lp_{600\ °C}} \tag{2}$$

With this strain and Young's modulus (Eq. 3), stress can be calculated using Hooke's law.

$$\sigma = E \bullet \varepsilon \tag{3}$$

The strains and film stresses calculated in this way are listed in Table 4.

The calculated film stresses are approximately −1.2 GPa and −1.3 GPa respectively. These values correspond very well with those that were determined in a previous study [15] using the Stoney equation [47] extended by Mézin [48] reporting a stress of −1.23 GPa for the TiO_2 films in the as-deposited state.

The TiO_2 films exhibit a slight texture. This is not particularly strong and could be mapped well with the March function [36]. The March parameter was in the range between 0.8 and 1.5, which indicates little to no texture. A change in texture due to the heat treatment could not be detected.

3.3.2. *Calcium cobalt oxide*

A diffraction image of an as-deposited 50 µm thick CCO-349 PAD film is shown in Fig. 13-a). The narrow, white concentric rings are reflections of the CCO.

It is clearly shown that the film is crystalline, which can be deduced from the presence of rings, i.e. reflections. From the ring shape and composition, something else can be noticed: Although only a 1 mm× 0.5 mm area of the 50 µm thick film was irradiated and the sample was also not rotated, the ring is uniformly bright. This means that, despite the small sample volume, there are enough crystals present and they are also distributed extremely homogeneously in the film plane to ensure this uniform exposure of the detector. Furthermore, the circles indicate a homogeneous distribution of a possible in-plane compressive stress in the film. Analogous to the section on TiO_2, the integrated diffractogram is shown in Fig. 13-b) from the diffraction image (black). This is shown with the background and the values calculated in the Rietveld refinement (red) as well as the calculated background curve (blue) and the difference between measured values and fit (orange) in Fig. 13-b).

Again, for better visibility the measured data (black) and the fitted data (red) are plotted in a separate diffractogram after the background has been subtracted. This is shown in Fig. 14.

In contrast to the TiO_2 films, the reflections appear narrower here, which is not typical for PAD, as these films usually have a small

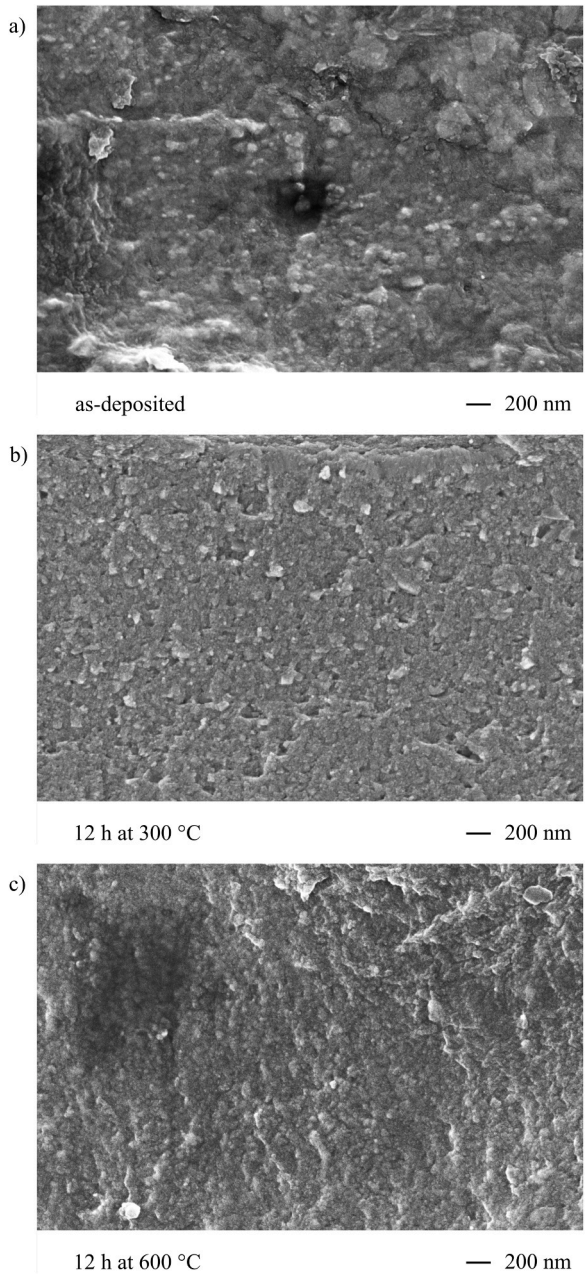

Fig. 9. SEM fracture images of TiO_2 PAD films in the as-deposited state (a), after heat treatment at 300 °C (b) and 600 °C (c).

crystallite size and a high microstrain. However, this matches the SEM fracture images in Fig. 10 showing significant bigger crystallite sizes compared to conventional PAD films exemplified by TiO_2 (see Fig. 9).

The numerical crystallite size values obtained from the refinement of CCO-349 are larger than the crystallite size that can be resolved with this setup. Therefore, the only statement that can be made at this point is that the crystallite size is already larger in the as-deposited state than can be resolved with this method (resolution limit of the setup: approx. 1 µm). This is very unusual for the powder aerosol deposition method. Typically, the crystallite size of PAD films is between 10 nm and 40 nm, as the crystallite sizes of the titanium oxide films shown before.

However, this is consistent with the SEM images, which show a microstructure that is very atypical for PAD films. According to this, the layer-like objects, which are several hundred nanometers in size, are actually individual CCO crystals. What is particularly interesting is that the crystals diffract coherently even at this full size. What we calculate as

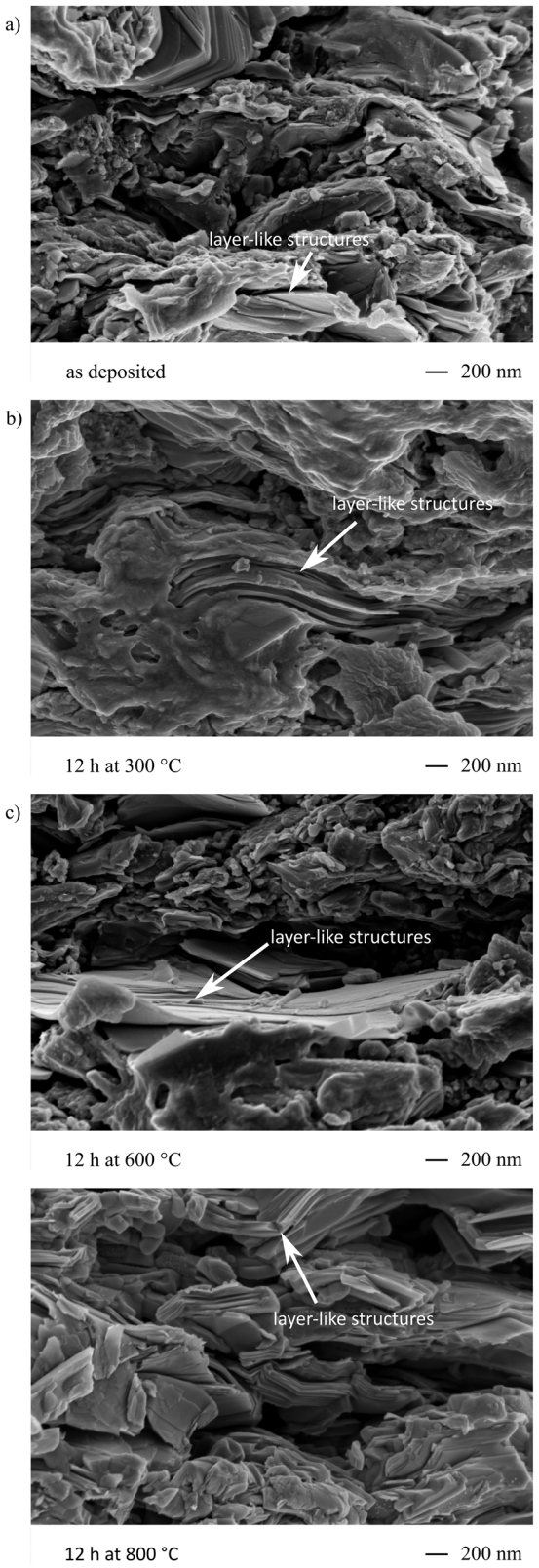

Fig. 10. SEM fracture images of CCO-349 PAD films in the as-deposited state (a), after heat treatment at 300 °C (b), 600 °C (c) and 800 °C (d).

L_{vol}-IB is actually not a crystallite size, but the size of a coherently diffracting domain in the crystal. One would actually expect the impact of the crystal on the substrate to create multiple kinks that divide these large crystals, visible in the fracture image, into small domains.

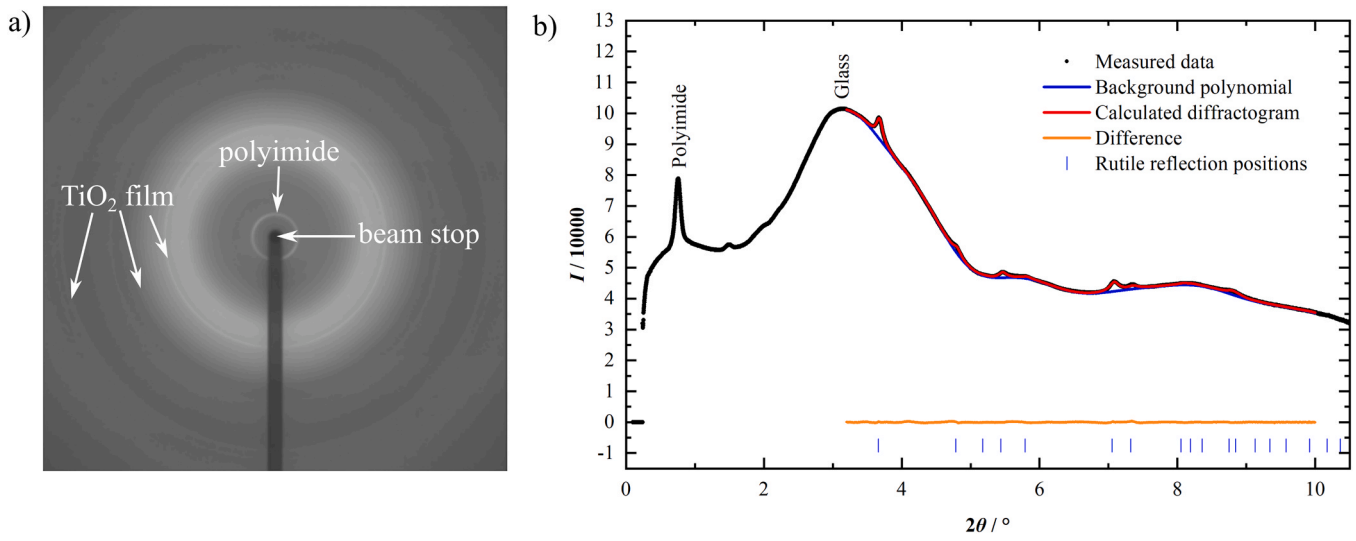

Fig. 11. Diffraction image of a 10 µm thick as-deposited TiO_2 PAD film on a soda-lime glass substrate as measured (a) and integrated by a 2D diffraction image (b). In (b) the integrated signal is shown in black. In addition, the data calculated by Rietveld refinement (red), as well as the background (blue) and the difference between calculated and measured data (orange) are shown.

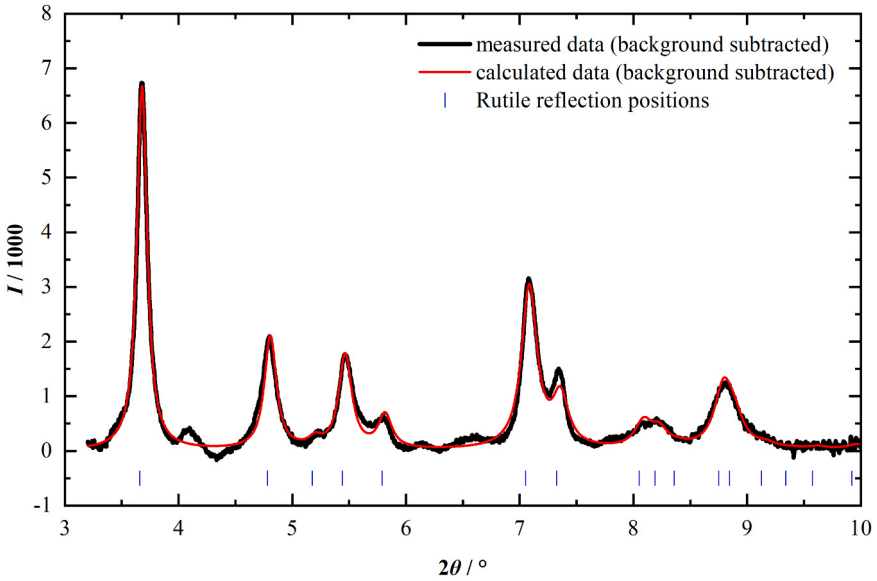

Fig. 12. Reflections of TiO_2 obtained by the data shown in Fig. 11 with subtracted background. Black are the measured data, red the calculated data. The *hkls* of the reflexes are also shown.

Table 2
Median of determined crystallite sizes and microstrains *E0* with 10th and 90th percentiles of different heat treated TiO_2 sample films.

Sample type	Crystallite sizes L_{vol}-IB / nm			Microstrain E0		
	Median	P10	P90	**Median**	P10	P90
powder*	**302**	-	-	**0.0006**	-	-
as-deposited	**19**	16	23	**0.0170**	0.0163	0.0186
300 °C	**14**	13	16	**0.0089**	0.0081	0.0118
600 °C	**14**	13	16	**0.0048**	0.0034	0.0063

(*only one sample was characterized)

According to the results of the X-ray diffraction, however, this is not the case.

The same applies to the starting powder. The crystallites are larger than the resolution limit of the beamline of approx. 1 µm. A strong reduction in the crystallite size due to the deposition process, as is usual with the PAD and as has also occurred with titanium oxide, has therefore not taken place in the case of CCO-349.

The values for the microstrain are listed for CCO-349 over the different post-treatment temperatures in Table 5.

At 0.012, the microstrain is slightly lower than that of TiO_2 in the as-deposited state. The microstrain shows the typical behavior of a PAD film during heat treatment. The as-deposited film has a microstrain of 0.012, which decreases to 0.005 after 1 h at 800 °C due to the heat treatment. In the case of CCO, this relaxation of the microstrain leads to a significant increase in conductivity. [15,28] It is also worth mentioning that the microstrain of the powder (0.0046) is significantly higher than the microstrain of the TiO_2 powder. It is also only slightly smaller than the microstrain of the samples treated at 800 °C.

The refined lattice parameters are listed in Table 6.

At this point, it should be pointed out that the lattice parameters a, b_1 and b_2 barely change as a result of the heat treatment. This means that

Table 3
Median of the lattice parameters *a* and c with 10th and 90th percentiles of different heat-treated TiO_2 films.

Sample type	*a* / Å			*c* / Å		
	Median	P10	P90	**Median**	P10	P90
powder*	4.593(1)	-	-	2.958(5)	-	-
as-deposited	4.571(4)	4.567(1)	4.576(3)	2.941(4)	2.939(7)	2.944(3)
300 °C	4.595(0)	4.591(5)	4.599(0)	2.953(2)	2.951(1)	2.955(7)
600 °C	4.591(6)	4.588(6)	4.596(0)	2.955(8)	2.953(9)	2.958(5)

(*only one sample was characterized)

Table 4
Lattice parameters of the as-deposited and heat-treated TiO_2 films with calculated strain and compressive stress.

Lattice parameter	as-deposited film in Å	Film annealed at 600 °C in Å	Calculated strain ε / %	Calculated intrinsic stress σ / GPa
a	4.57140	4.59163	-0.4405	-1.178
c	2.94144	2.95583	-0.4868	-1.301

there is hardly any compressive stress in the CCO-349 layer. This is a significant difference to TiO_2, which has a very high intrinsic compressive stress of −1.2 GPa.

Similar to Nakamura et al. [18] and Yoon et al. [16], as well as in our previous study [17], the SEM of CCO-349 already indicated a strong fiber texture. In the Debeye-Scherer-like setup, this is not as evident as in the diffractogram obtained in the Bragg-Brentano setup, in which only (0 0 *l*) reflexes are present. However, it was only possible to realize the complex texture reasonably satisfactorily by imaging with eighth-order spherical harmonics in the Rietveld refinement. Based on the previous investigations [17] and the SEM investigations, we continue to assume a fiber texture. However, the texture is too complex to draw reliable conclusions from the available data.

4. Discussion

4.1. Film morphology, intrinsic compressive stress, and annealing

With regard to the microstructure, there are significant differences between the films even in the as-deposited state. While the crystallite size of TiO_2 is in the typical PAD range of 10 nm to 30 nm, the crystals of CCO-349 are larger than the 1 µm that can be resolved by the measurement setup.

The microstrain differs slightly for both materials in the as-deposited state, but it is relatively high for both materials, which is very typical for PAD. The TiO_2 films show a PAD-typical high intrinsic compressive stress of −1.2 GPa, while the CCO-349 films are almost stress-free after deposition. In addition to the barely pronounced texture of the film in TiO_2, the strong fiber texture of CCO-349 is another significant difference between the film properties of the two materials.

The films behave similarly during heat treatment. The microstrain decreases in both materials. In the case of TiO_2, the intrinsic compressive stress also relaxes. In the case of CCO-349, this cannot relax as it is already absent in the as-deposited state.

The microstructure of CCO-349 films deposited by means of PAD, as elucidated in this study (compare Fig. 10), has some peculiarities that strongly indicate that the deposition process must be different from TiO_2 and other conventionally PAD-deposited films. This would be, for example, the strong fiber texture, the large crystallite size, and the low intrinsic compressive stress (compare Table 5).

This shows that crystallite size and intrinsic compressive film stress, as well as the microstrain, are film properties that are apparently material-specific and can be linked to the powder crystallite size and morphology.

4.2. Film deposition mechanism for polycrystalline particles without layered crystal structure

Based on the RTIC mechanism described by Akedo [7] and its extension by Linz et al. [11], we will now try to explain how these different film properties or morphologies can occur. Imagine a polycrystalline particle hitting a surface at very high speed (Fig. 15 a)) as it is

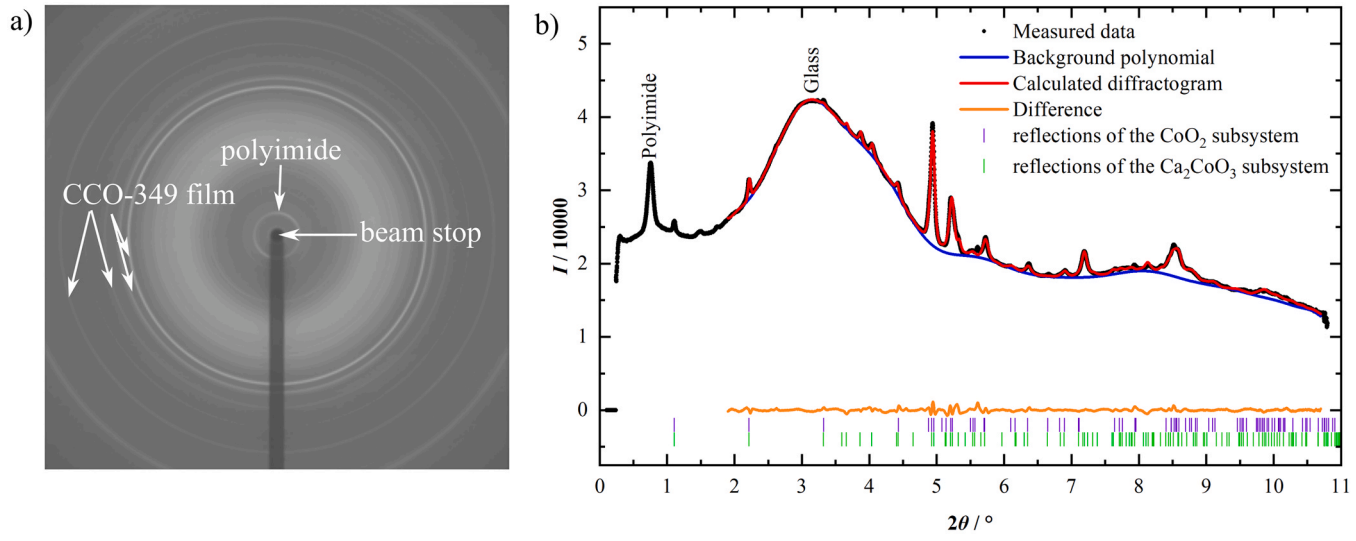

Fig. 13. Diffraction image of a 50 µm thick as-deposited CCO-349 PAD film on a soda-lime glass substrate as measured (a) and integrated by a 2D diffraction image (b). In (b) the integrated signal is shown in black. In addition, the data calculated by Rietveld refinement (red), as well as the background (blue) and the difference between calculated and measured data (gray) are shown.

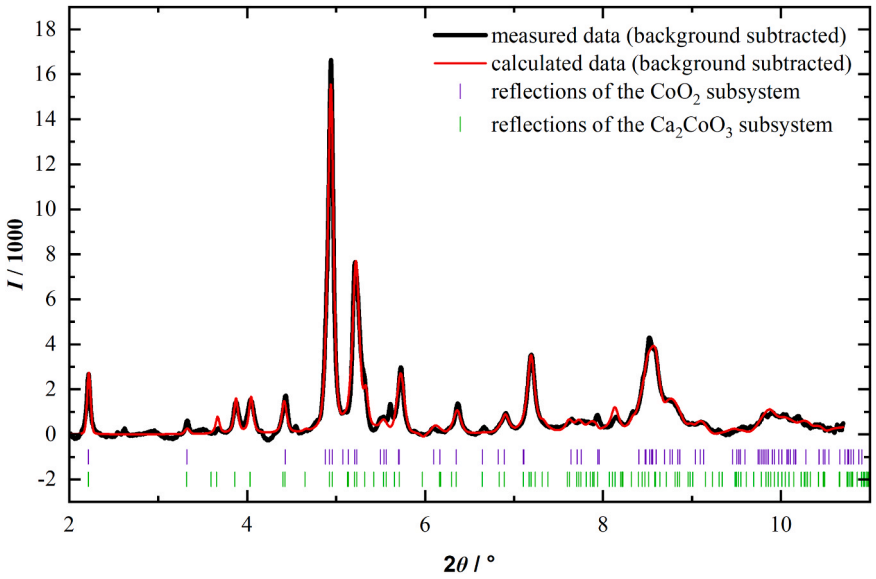

Fig. 14. The data shown in Fig. 13 with subtracted background. Black are the measured data, red the calculated data. We have refined from entering the *hkls* here, as this is not possible in a clear manner due to the large number of individual reflections that overlap to form larger reflections.

Table 5
Microstrain in CCO-349 films for the different heat treatment temperatures.

Sample type	Median	P10	P90
powder*	**0.00460**	-	-
RT	**0.01202**	0.01168	0.01293
300 °C	**0.01096**	0.01014	0.01200
600 °C	**0.00708**	0.00699	0.00722
800 °C**	**0.00513**	-	-

(*only one sample was characterized)
(*There are only two values for this sample type, so the arithmetic mean is given instead of the median.)

the case during deposition of TiO_2. On impact, the lower part of this particle will dig into the surface it hits (Fig. 15 b) and c)). It will expand the surface like a wedge, creating compressive stress. This compressive stress depends on the yield strength of the deposited material [15]. Due to the high energy input, plastic deformation will occur both in the impacted surface and in the lower part of the polycrystalline particle. The fact that plastic deformation can occur in such small ceramic particles has been frequently demonstrated in the literature. [7,50] Depending on the structure and defect density of the crystals on the surface of the substrate or on the already deposited film or particle, a more or less plastic deformation is possible. If plastic deformation is no longer possible, the crystals break. Likewise, so much plastic deformation can occur that the long-range order of these crystals is disturbed to such an extent that instead of one, there are many different coherent diffracting domains. Fracture and deformation now create a form fit between the lower part of the particle and the surface on which it has impacted. Furthermore, the part that has dug into the surface is trapped by the film stress that it has generated itself.

There are contradictory observations in the literature as to whether this energy input leads to a partial amorphization of the material. While Yang et al. [46] identify amorphous areas in the material on their TEM images, Akedo [7] reports that no such areas occur. This may also depend on the deposited material. In any case, it is not possible to detect the presence or absence of amorphous regions with the X-ray diffraction setup used here. One reason for this is that these small areas would already diffract weakly due to their small proportion of the sample and this low intensity would then also be distributed over a very wide halo, which would still overlap with the glass substrate used.

In any case, there is a strong increase in the defect density, which can be assessed using the microstrain. This is a measure of the irregularity of the lattice parameters and increases with an increase in the defect density, as the stress fields around the defects cause a local distortion of the crystal lattice.

However, the extent to which the deposited crystals can be deformed at the direct contact surface depends not only on their structure, but also on the applied energy. This depends on the one hand on the mass of the impinging particle and on the other hand on its speed. It is important how much of this energy is ultimately introduced into the volume that participates in the deposition, i.e., on the few crystallites directly at the point of contact between the particle and the substrate surface [11]. The momentum of the entire impacting particle is conducted towards the substrate during the impact via the primary crystals of the particle and, above all, via the joints between them. The force is transmitted via pressure or thrust, depending on the position in the particle. The strength of the primary crystals, and above all their contact points, therefore determines how much force is transferred to the immediate impact volume.

During impact, the bonds between the primary crystals partially fail and the outer part of the particle is separated. The majority of the particle that does not adhere to the surface or is strongly compacted is removed by the downstream carrier gas (Fig. 15 d)). Lee et al. [51] suggest that at least some of these particles remain attached to the surface for some time. They would then be further compacted by subsequent particles and become part of the film (hammering effect [7]), or they are knocked away from the surface by a subsequent particle and removed by the carrier gas flow.

4.3. Film deposition mechanism for materials with layered crystal structure

The question now is how the large crystallites in CCO-349 can occur in the as-deposited state if the particles have to be broken up for deposition. In contrast to TiO_2, CCO-349 consists of much bigger crystallites (compare Fig. 10), which can be considered as single crystals. So, there are no small primary crystals that are small enough to be plastically deformed [7] and that can penetrate a surface and the bond to the rest of the particle cannot break off so easily. Accordingly, the consequence would be that such particles would deposit less easily or not at all. A publication by Naoe et al. [52] has shown that. Polycrystalline particles deposit better than singlecrystalline particles. However, the comparison

Table 6
Lattice parameters of the CCO-349 in the PAD film in the as-deposited state and after heat treatment.

Lattice parameter	Sample type	Median	P10	P90	Muguerra et al. [39]
	powder*	**4.831(7)**	-	-	
	as-deposited	**4.831(2)**	4.83023	4.83230	
a / Å	300 °C	**4.830(1)**	4.82898	4.83190	4.8395
	600 °C	**4.833(0)**	4.83196	4.83399	
	800 °C*	**4.831(3)**	-	-	
	powder*	**2.822(2)**	-	-	
	as-deposited	**2.820(8)**	2.82052	2.82117	
b_1 / Å	300 °C	**2.819(6)**	2.81902	2.81997	2.8019
	600 °C	**2.820(2)**	2.81979	2.82061	
	800 °C*	**2.820(8)**	-	-	
	powder*	**4.569(8)**	-	-	
	as-deposited	**4.562(6)**	4.56080	4.56471	
b_2 / Å	300 °C	**4.567(0)**	4.56531	4.56928	4.5531
	600 °C	**4.556(9)**	4.55604	4.55785	
	800 °C**	**4.562(8)**	-	-	
	powder*	**10.84(4)**	-	-	
	as-deposited	**10.84(4)**	10.84352	10.84359	
c_1 / Å	300 °C	**10.84(3)**	10.84328	10.84332	10.8583
	600 °C	**10.84(4)**	10.84377	10.84392	
	800 °C**	**10.84(4)**	-	-	
	powder*	**10.84(4)**	-	-	
	as-deposited	**10.84(4)**	10.84346	10.84362	
c_2 / Å	300 °C	**10.84(3)**	10.84310	10.84319	10.8583
	600 °C	**10.84(3)**	10.84355	10.84366	
	800 °C**	**10.84(3)**	-	-	
	powder*	**98.14(1)**	-	-	
	as-deposited	**98.14(1)**	98.14107	98.14108	
β_1 / °	300 °C	**98.14(1)**	98.14107	98.14107	98.124
	600 °C	**98.14(1)**	98.14106	98.14107	
	800 °C**	**98.14(1)**	-	-	
	powder*	**98.14(1)**	-	-	
	as-deposited	**98.14(1)**	98.14107	98.14108	
β_2 / °	300 °C	**98.14(1)**	98.14108	98.14109	98.124
	600 °C	**98.14(1)**	98.14108	98.14109	
	800 °C**	**98.14(1)**	-	-	

(*only one sample was characterized)
(**There are only two values for this sample type, so the arithmetic mean is given instead of the median)

between TiO_2 and CCO-349 has shown exactly the opposite here.

How can we now integrate these characteristics of CCO-349 into the model for the deposition mechanism? Firstly, the different particle morphology of the powders should be noted. The CCO-349 powder consists of relatively large particles with big primary crystals (see Fig. 6). For aluminum oxide, it could be shown that large, monocrystalline particles are usually rather unsuitable for deposition [52]. However, this does not seem to apply to CCO-349. Although the particles are not completely monocrystalline, they consist of very few individual crystals. A different particle morphology naturally leads to a different introduction of force into the contact area between the particle and the substrate surface. The influence of the bond between the primary crystals is almost completely eliminated in such a powder. It should also be mentioned that a titanium oxide with a similarly large particle size distribution would probably not deposit at all.

The second and very significant difference between CCO-349 and conventional materials for the aerosol deposition lies in their crystal structure. Commonly used materials have a high or very high symmetry. Typical representatives here would be cubic MgO [15] with the space group P42/mnm or cubic LLZO [53] with the space group Ia-3d with very high symmetry. Systems with high symmetry would be tetragonal systems, such as titanium oxide [15] or barium titanate [40,43] or trigonal systems such as α-aluminum oxide [29,44,45]. A high degree of symmetry in the crystal generally also increases the number of available mechanical slip systems, which is a precondition for plastic deformation, that happens during deposition, as shown in [7]. In CCO-349, however, the number of slip systems is greatly reduced by the incommensurable crystal structure. This is because the misfit imposes the condition that the slip plane must not intersect the plane of the misfit, or in other words, the nominal vector of the slip plane must be perpendicular to the vectors $\boldsymbol{b_1}$ and $\boldsymbol{b_2}$.

This means, that only the plane (0 0 1) is available in CCO-349. All dislocations in other slip planes would require a Burgers vector for a dislocation that is at least as long as the lattice parameter $\boldsymbol{c}$ with a length of 10.85 Å. This would be extremely unfavorable from an energy perspective.

In the slip plane (0 0 1), there are various slip systems that can be divided into two groups. One group is formed by slip systems that are subject to typical Schmid deformation. For the hexagonal CoO_2 system, for example, this would be $\{0\ 0\ 1\} < 1\ 1\ 0 >$ or for the cubic Ca_2CoO_3 system it is $\{0\ 0\ 1\} < 2\ 1\ 0 >$. The subsystems are shifted by a defined proportion of the unit cell so that the cell looks like it did before the deformation.

The second group forms the system $(0\ 0\ 1) < 0\ 1\ 0 >$ for both subsystems. This represents a shift in the direction of the misfit. This system will undoubtedly be the preferred system in the crystal, as no position of the subsystems to each other is defined due to the misfit and they can simply slide away from each other.

An example of the crystal deforming by sliding across this plane or even splitting preferentially there was found when the particles were examined by SEM. One particle has been partially compressed. This is shown in Fig. 7. The deformation of the crystal can be seen by sliding on the planes.

Let's now take a single CCO-349 particle consisting of few big single crystals. Due to its habitus, CCO forms particles that have the shape of more or less thick disks (see Fig. 6). If such a particle hits a substrate surface, it can adapt relatively well to the geometry of the substrate surface by plastic deformation, in which the layers of the subsystems

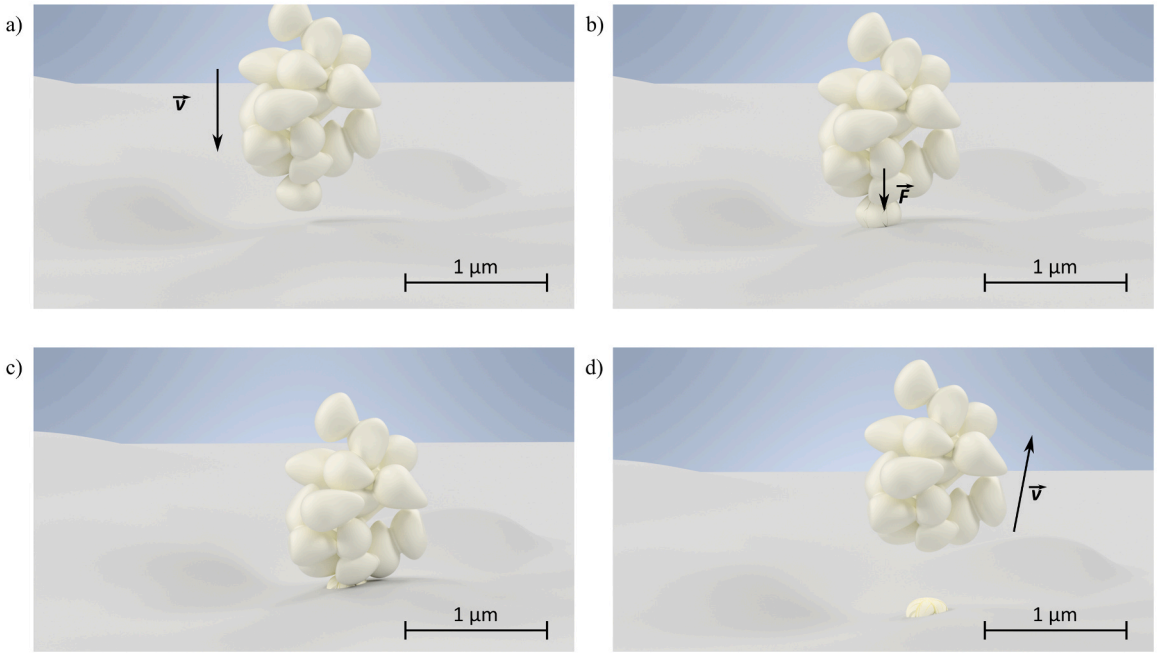

Fig. 15. Scheme of the deposition mechanism for materials without layered crystal structure. A particle moves towards the substrate at high speed a). On contact with the substrate surface, the force generated by the change in momentum of the particle is transferred to the primary crystal in contact with the substrate surface b). This leads to plastic deformation of this crystal and to break-up. It is also pressed into the substrate surface by the forces acting on it c). At the same time, the bonds to the other primary crystals break. The particle is carried away by the gas flow and the deposited crystallite is hammered by subsequent particles and further deformed or compacted d) (hammering effect [7]).

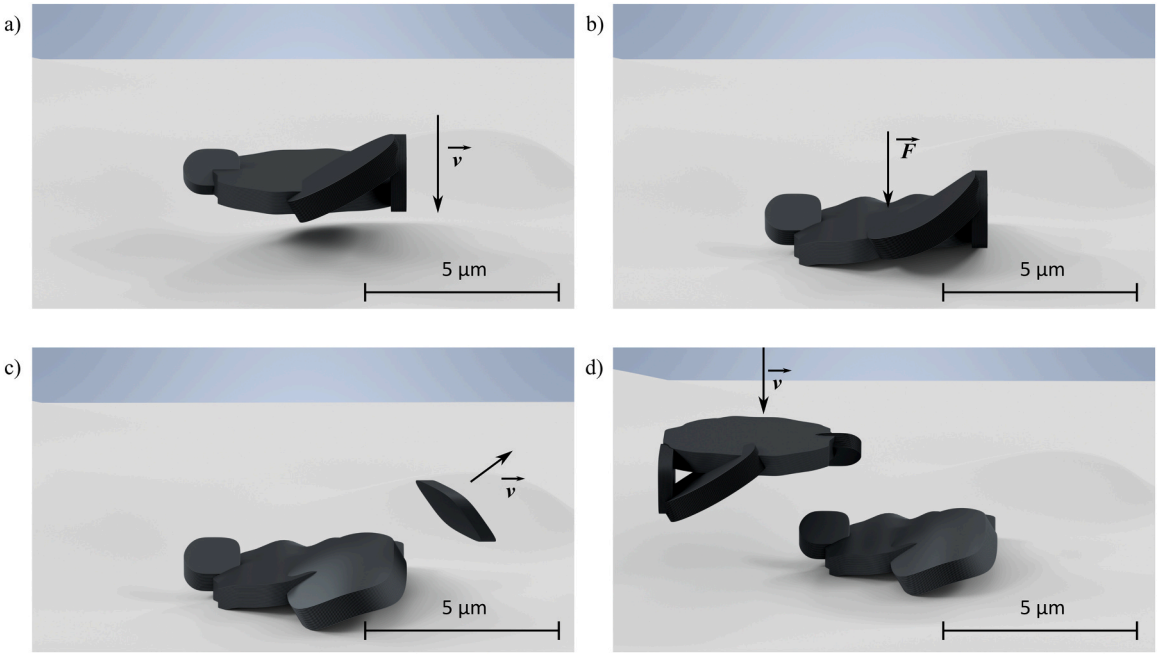

Fig. 16. A CCO-349 particle moves towards the substrate, accelerated by the carrier gas a). When it hits the substrate, it can adapt to the surface of the substrate by deformation b) and c). The deformation occurs by sliding along the basal plane. Parts that are unfavorably oriented and cannot deform in this way break out c). Compaction takes place via further, subsequent particles d).

slide away from each other. This can be imagined as a stack of paper that falls to the floor or is placed on an uneven surface. By sliding the paper sheets, this stack will adapt to the surface. This mechanism is shown as an example in Fig. 16 a) - d).

Even if this stack is not parallel to the surface, but the sheets are tilted at a certain angle to the surface, this mechanism will result in the sheets of the stack lying largely flat on the floor, provided the angle is not too steep. This could explain the formation of the microstructure as shown in the SEM images in Fig. 10

Since CCO-349 particles synthesized by the method presented here consist of several big crystals, it is also possible that only a smaller crystal matching the deformation mechanism occurs. This case is shown in Fig. 17. In this case, only the small part that can adapt to the surface via the deformation mechanism presented above would be deposited.

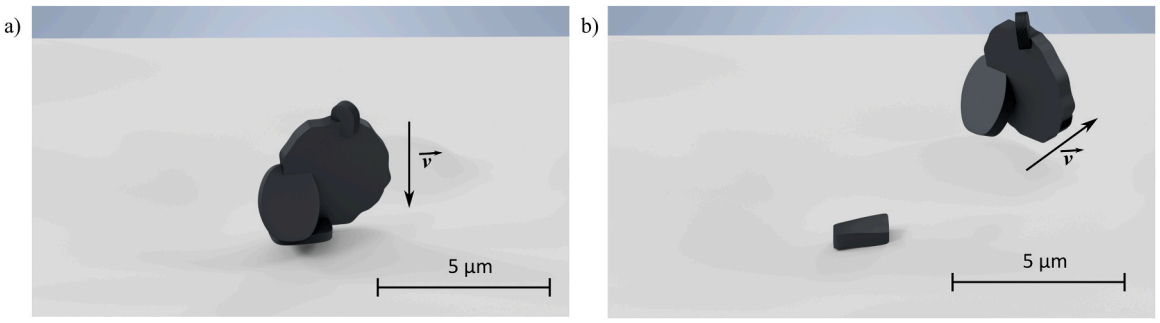

Fig. 17. A CCO-349 particle hits (a) with a different orientation. Only a small part can deform well, the test breaks off and is carried away by the carrier gas flow.

The rest of the particle would break off and be carried away by the carrier gas flow.

This model is supported by the fact that it can explain the large crystallite size in the deposited film, as it enables a sufficiently large plastic deformation and actual breaking of the particles is no longer necessary. This model would also explain the strong fiber texture that occurs, which is rather unusual for PAD. If one now also considers that this other deposition mechanism should generate a lower intrinsic compressive stress due to a higher adaptation of the impinging particle to the substrate surface, because it naturally digs less deeply into the material, this observation also fits into the picture.

From this point of view, it is also interesting that some parallels can be observed if one refers to a publication on another material that also has a layered structure. A representative of this would be Ti_3SiC_2, which was deposited and investigated by Henon et al. [54]. In contrast to CCO-349, however, this material has no misfit in its layers, i.e., it consists of a commensurate structure of space group P63/mmc. In other words, a hexagonal crystal structure in which layers of TiC and weaker bonded Si alternate. Here, too, one might expect a sliding of the basal plane (or of dislocations in the basal plane) rather than in other slip planes of this structure. TEM images in the paper by Henon et al. clearly show a strong fiber texture as present in CCO-349 in this paper. However, the film of Henon et al. had a much smaller crystallite size. Nevertheless, we see parallels here that strongly indicate that a layer-like structure of a crystal structure has an immense influence on what happens in detail during deposition.

According to the mechanism just presented, however, only a deformation or sliding of the layers in one direction, namely in the (0 *k* 0) direction, i.e., the direction of the misfit, would be particularly favored. This would also be possible in all other directions, but only through Schmid deformation. Bending around the ***a***-axis would therefore be preferred.

The results of Suzuki et al. [55], who investigated the texture of commensurate layered bismuth titanate, are also extremely interesting at this point. They observed a strong texture in thin films, which decreases with increasing film thickness, i.e., consequently with increasing distance from the substrate. The strength of the texture in thin films depends on the synthesis route used to produce the powder and therefore also on the particle geometry and crystallite form.

Barely textured films of materials with a commensurate layered crystal structure are also obtained with Bi_2Te_3[56], with a relatively high deposition rate. Whether this texture changes over the film thickness as with Suzuki cannot be determined from the data, as the penetration depth of Cu-$K_{\alpha 1}$ radiation is not particularly high in strong scattering materials like Bi_2Te_3.

However, no decrease in texture with increasing film thickness can be detected in the films investigated in this work. Even with XRD in reflection geometry, the areas near the surface of thick films are highly textured. [17] This leads to the assumption that the constant texture only occurs in materials with an incommensurate layered crystal structure.

4.4. Surface condition effect on film formation

It makes a difference whether the particles hit an uncoated substrate or an already deposited film. The surface condition determines the ability of the particles to allow some of their primary crystals to penetrate the surface due to the force acting during the impact. This is much easier with an already existing, nanocrystalline and therefore ductile film than with an uncoated substrate. With uncoated substrates, the hardness and surface properties, i.e., the roughness and microstructure of the surface, play a role. A particle can penetrate a hard surface much less easily and leave some of its primary crystals firmly anchored there than on a soft surface. This leads to a lower film formation rate and presumably also to a changed film morphology, which in turn influences the deposition of a further layer. This is the reason why Schubert et al. [57] found an influence of the substrate hardness and roughness on the film formation.

The roughness of the surface also plays a role, as the angle at which the particles hit the surface naturally makes a difference to the forces acting and transmitted during impact. A recent publication by Yang et al. [46] investigated the microstructure of an Al_2O_3 PAD film on a structured Si substrate. The results fit well with the theory presented here. Looking only at the microstructure obtained by Yang et al. on the peaks of the Si pillars, one comes close to the structure that takes place during deposition on a smooth substrate.

Yang et al. found a 20 nm to 30 nm wide interface of amorphous Si between the substrate and the PAD film. The amorphization must have taken place at the beginning of the filmformation due to a high energy input until a layer was formed. Above this, crystallites in the size range 10–30 nm are found, which are randomly oriented. Similar to the TiO_2 in this study, Yang et al. [46] show the intrinsic compressive film stress, which has deformed the actually round halos that are formed when electrons are diffracted by amorphous material into ovals. The intrinsic stress reduces the atomic spacing in the in-plane direction. This influences the scattering.

With thick films of CCO-349 on smooth glass, we also found that the films detached from the barely changed substrate. Roughening and penetration of the particles into the substrate surface does not occur when this material is deposited.

To summarize, for materials that resemble TiO_2, the size of the primary crystals and the bonding of the primary crystals influence the deposition in addition to the particle size. The way in which the starting material was produced is therefore essential here, as it essentially defines the particle morphology. The specific material is also crucial, as this determines how the primary crystals can deform or break. If we are very far away from the deformation behavior of rutile crystals, this may result in a different deposition mechanism, as it is the case with CCO-349.

5. Summary

In this work a comprehensive characterization of the powder and

microstructure of powder aerosol deposited films of TiO_2 and CCO-349 by SEM at fracture surfaces and hard x-ray diffractometry with synchrotron radiation and sequential Rietveld refinement has been performed. The titanium oxide films were used to validate many previously obtained results [15] using high-quality data. Based on the RTIC model from Akedo [7] and its extension by Linz et al. [11] from the literature, a model for a deposition mechanism for TiO_2 material has been presented. The deposition behavior and film properties, such as residual strains, morphology including crystal size, and texture, were correlated to the morphology of the starting powder to be deposited.

Investigations of films made from misfit-layered incommensurate CCO-349 showed that this material has a different microstructure. Due to this significantly different microstructure, it was concluded that the formation of a different microstructure must be based on a different deposition mechanism. The ability for plastic deformation of powder particle and surface were considered as being crucial for film deposition.

Polycrystalline titanium oxide powder particles consisting of several grains per particle form films by deformation and breaking of some primary crystals of the powder particle.

A certain amount of plastic deformation is necessary to create a form-fitting connection to the adjacent material. Ceramic materials such as titanium oxide can also achieve this, but only to a certain extent; the remaining geometric adjustment of the material can only be achieved by breaking.

CCO-349 has a better possibility to deform as a single crystal due to its misfit-layered structure. Due to its crystal structure, CCO-349 can be deformed more easily than conventional technical ceramics. The deformation occurs when the layers in the crystal slide in the direction of the misfit. This can be imagined as bending a stack of paper. As a result, it is no longer necessary to break the crystals, and a larger crystallite size remains in the film. Therefore, PAD films of CCO-349 have a different microstructure with larger crystallites and a strong fiber texture.

CRediT authorship contribution statement

Ralf Moos: Writing – review & editing, Supervision, Funding acquisition. **Sander van Smaalen:** Writing – review & editing, Supervision, Formal analysis. **Anna Lena Hansen:** Writing – review & editing, Funding acquisition, Data curation. **Mario Linz:** Writing – review & editing, Conceptualization. **Daniel Paulus:** Writing – original draft, Investigation, Formal analysis, Data curation, Conceptualization. **Daniela Schönauer-Kamin:** Writing – review & editing, Supervision, Project administration, Funding acquisition, Conceptualization. **Anke Silvia Ulrich:** Writing – review & editing, Supervision, Conceptualization.

Declaration of Competing Interest

The authors declare that they have no known competing financial interests or personal relationships that could have appeared to influence the work reported in this paper.

Acknowledgements

We acknowledge DESY (Hamburg, Germany), a member of the Helmholtz Association HGF, for the provision of experimental facilities. Parts of this research were carried out at PETRA III and we would like to thank Dr. Volodymyr Baran for assistance in using beamline P02.1. Beamtime was allocated for proposal I-20230953 and proposal I-20240866. We acknowledge the KeyLab Electron and Optical Microscopy (Bayreuth, Germany), a KeyLab of the Bavarian Polymer Institute (BPI), for the provision of SEM (Zeiss LEO 1530). We would like to thank Ulrich Mansfeld and Martina Heider for assistance in using the SEM. We would like to thank the Chair of Applied Mechanics and Fluid Mechanics at the University of Bayreuth (J. Sesterhenn), especially Gabi Jena, for measuring the particle size distribution. We would also like to thank John Evans for providing many valuable resources and scripts on Topas wiki (https://topas.awh.durham.ac.uk/) that were particularly valuable in analyzing the synchrotron data. The authors would like to thank the DFG. Parts of the research presented here were funded by the Deutsche Forschungsgemeinschaft (DFG, German Research Foundation) – 544448150. The authors would like to thank the German Federal Ministry of Education and Research (BMBF) within the framework of the FestBatt2 cluster (BMBF grant 03XP0441A) and the Bavarian Center for Battery Technology (BayBatt) for funding parts of the research for this work.

Appendix A. Supporting information

Supplementary data associated with this article can be found in the online version at doi:10.1016/j.jeurceramsoc.2026.118127.

References

[1] S. Kashu, E. Fuchita, T. Manabe, C. Hayashi, Deposition of ultra fine particles using a gas jet, Jpn. J. Appl. Phys. 23 (1984) 910–912, https://doi.org/10.1143/JJAP.23.L910.
[2] J. Akedo, M. Ichiki, K. Kikuchi, R. Maeda, Jet molding system for realization of three-dimensional micro-structures, Sens. Actuator A Phys. 69 (1998) 106–112, https://doi.org/10.1016/S0924-4247(98)00059-4.
[3] M. Ichiki, J. Akedo, A. Schroth, R. Maeda, Y. Ishikawa, X-ray diffraction and scanning electron microscopy observation of lead zirconate titanate thick film formed by gas deposition method, Jpn. J. Appl. Phys. 36 (1997) 5815–5819, https://doi.org/10.1143/JJAP.36.5815.
[4] J. Akedo, Room temperature impact consolidation (RTIC) of fine ceramic powder by aerosol deposition method and applications to microdevices, J. Therm. Spray. Tech. 17 (2008) 181–198, https://doi.org/10.1007/s11666-008-9163-7.
[5] J. Akedo, Aerosol deposition of ceramic thick films at room temperature: densification mechanism of ceramic layers, J. Am. Ceram. Soc. 89 (2006) 1834–1839, https://doi.org/10.1111/j.1551-2916.2006.01030.x.
[6] J. Akedo, Aerosol deposition method for fabrication of nano crystal ceramic layer, MSF 449-452 (2004) 43–48, https://doi.org/10.4028/www.scientific.net/MSF.449-452.43.
[7] J. Akedo, Room temperature impact consolidation and application to ceramic coatings: aerosol deposition method, J. Ceram. Soc. Jpn. 128 (2020) 101–116, https://doi.org/10.2109/jcersj2.19196.
[8] J. Akedo, M. Lebedev, S. Baba, Aerosol deposition method for preparation of lead zirconate titanate thick layer at low temperature –improvement of electrical properties by irradiation of fast atom beam and plasma, Jpn. J. Appl. Phys. 42 (2003) 5931–5935, https://doi.org/10.1143/JJAP.42.5931.
[9] J. Akedo, S. Nakano, J. Park, S. Baba, K. Ashida, The aerosol deposition method, Synth. Engl. Ed. 1 (2008) 121–130, https://doi.org/10.5571/syntheng.1.121.
[10] S. Baba, L. Huang, H. Sato, R. Funahashi, J. Akedo, Room-temperature fast deposition and characterization of nanocrystalline Bi 0.4 Sb 1.6 Te 3 thick films by aerosol deposition, J. Phys. Conf. Ser. 379 (2012) 12011, https://doi.org/10.1088/1742-6596/379/1/012011.
[11] M. Linz, F. Bühner, D. Paulus, L. Hennerici, Y. Guo, V. Mereacre, U. Mansfeld, M. Seipenbusch, J. Kita, R. Moos, Revealing the deposition mechanism of the powder aerosol deposition method using ceramic oxide core-shell particles, Adv. Mater. 36 (2023) e2308294, https://doi.org/10.1002/adma.202308294.
[12] J. Exner, M. Hahn, M. Schubert, D. Hanft, P. Fuierer, R. Moos, Powder requirements for aerosol deposition of alumina films, Adv. Powder Technol. 26 (2015) 1143–1151, https://doi.org/10.1016/j.apt.2015.05.016.
[13] J. Exner, M. Schubert, D. Hanft, J. Kita, R. Moos, How to treat powders for the room temperature aerosol deposition method to avoid porous, low strength ceramic films, J. Eur. Ceram. Soc. 39 (2019) 592–600, https://doi.org/10.1016/j.jeurceramsoc.2018.08.008.
[14] D. Hanft, J. Exner, M. Schubert, T. Stöcker, P. Fuirer, R. Moos, An overview of the aerosol deposition method: process fundamentals and new trends in materials applications, J. Ceram. Sci. Technol. 6 (2015) 147–182, https://doi.org/10.4416/JCST2015-00018.
[15] D. Paulus, J. Kita, R. Moos, Relaxation behavior of intrinsic compressive stress in powder aerosol co-deposited films: rethinking PAD films as nanomaterials, Ceram. Int. 49 (2023) 38375–38381, https://doi.org/10.1016/j.ceramint.2023.09.065.
[16] W.-H. Yoon, J. Ryu, J.-J. Choi, B.-D. Hahn, J.H. Choi, B.-K. Lee, J.-H. Cho, D.-S. Park, Enhanced thermoelectric properties of textured $Ca_3Co_4O_9$ thick film by aerosol deposition, J. Am. Ceram. Soc. 93 (2010) 2125–2127, https://doi.org/10.1111/j.1551-2916.2010.03674.x.
[17] D. Paulus, S. Bresch, R. Moos, D. Schönauer-Kamin, Powder aerosol deposited calcium cobaltite as textured P-type thermoelectric material with power factors approaching single crystal values, J. Eur. Ceram. Soc. 44 (2024) 116717, https://doi.org/10.1016/j.jeurceramsoc.2024.116717.
[18] Y. Nakamura, Y. Matsufuji, M. Inoue, Fabrication and properties of thermoelectric oxide thick films deposited with aerosol deposition method, J. Phys. Conf. Ser. 352 (2012) 12026, https://doi.org/10.1088/1742-6596/352/1/012026.
[19] M. Hasegawa, M. Komuro, K. Kimura, S. Hasimoto, M. Tanaka, S. Kitaoka, Y. Kagawa, Formation mechanism of texture in α-alumina coatings produced by

aerosol deposition, J. Ceram. Soc. Jpn. 129 (2021) 7–16, https://doi.org/10.2109/jcersj2.20135.
[20] Y. Furuya, S. Konuma, M. Hasegawa, Deposition mechanism of alumina particles in aerosol deposition based on the kinetic energy of particles, Surf. Coat. Technol. 458 (2023) 129362, https://doi.org/10.1016/j.surfcoat.2023.129362.
[21] A.C. Masset, C. Michel, A. Maignan, M. Hervieu, O. Toulemonde, F. Studer, B. Raveau, J. Hejtmanek, Misfit-layered cobaltite with an anisotropic giant magnetoresistance: $Ca_3Co_4O_9$, Phys. Rev. B 62 (2000) 166–175, https://doi.org/10.1103/PhysRevB.62.166.
[22] C.D. Ling, K. Aivazian, S. Schmid, P. Jensen, Structural investigation of oxygen non-stoichiometry and cation doping in misfit-layered thermoelectric $(Ca_2CoO_{3-x})(CoO_2)_\delta$, $\delta \approx 1.61$, J. Solid State Chem. 180 (2007) 1446–1455, https://doi.org/10.1016/j.jssc.2007.02.016.
[23] Y. Miyazaki, M. Onoda, T. Oku, M. Kikuchi, Y. Ishii, Y. Ono, Y. Morii, T. Kajitani, Modulated structure of the thermoelectric compound $[Ca_2CoO_3]_{0.62}\ CoO_2$, J. Phys. Soc. Jpn. 71 (2002) 491–497, https://doi.org/10.1143/JPSJ.71.491.
[24] J. Yu, R. Freer, Calcium cobaltite, a promising oxide for energy harvesting: effective strategies toward enhanced thermoelectric performance, J. Phys. Energy 4 (2022) 22001, https://doi.org/10.1088/2515-7655/ac5172.
[25] J. Yu, K. Chen, F. Azough, D.T. Alvarez-Ruiz, M.J. Reece, R. Freer, Enhancing the thermoelectric performance of calcium cobaltite ceramics by tuning composition and processing, ACS Appl. Mater. Interfaces 12 (2020) 47634–47646, https://doi.org/10.1021/acsami.0c14916.
[26] S. Bhattacharya, D.K. Aswal, A. Singh, C. Thinaharan, N. Kulkarni, S.K. Gupta, J. V. Yakhmi, Anisotropic electrical transport studies of $Ca_3Co_4O_9$ single crystals grown by the flux method, J. Cryst. Growth 277 (2005) 246–251, https://doi.org/10.1016/j.jcrysgro.2004.12.142.
[27] A.-C. Dippel, H.-P. Liermann, J.T. Delitz, P. Walter, H. Schulte-Schrepping, O. H. Seeck, H. Franz, Beamline P02.1 at PETRA III for high-resolution and high-energy powder diffraction, J. Synchrotron Rad. 22 (2015) 675–687, https://doi.org/10.1107/s1600577515002222.
[28] J. Exner, T. Nazarenus, D. Hanft, J. Kita, R. Moos, What happens during thermal post-treatment of powder aerosol deposited functional ceramic films? Explanations based on an experiment-enhanced literature survey, Adv. Mater. 32 (2020) e1908104, https://doi.org/10.1002/adma.201908104.
[29] M. Schubert, J. Exner, R. Moos, Influence of carrier gas composition on the stress of Al_2O_3 coatings prepared by the aerosol deposition method, Materials 7 (2014) 5633–5642, https://doi.org/10.3390/ma7085633.
[30] J. Adamczyk, P. Fuirer, Compressive stress in nano-crystalline titanium dioxide films by aerosol deposition, Surf. Coat. Technol. 350 (2018) 542–549, https://doi.org/10.1016/j.surfcoat.2018.07.015.
[31] N.H. Khansur, U. Eckstein, K. Riess, A. Martin, J. Drnec, U. Deisinger, K.G. Webber, Synchrotron x-ray microdiffraction study of residual stresses in BaTiO3 films deposited at room temperature by aerosol deposition, Scr. Mater. 157 (2018) 86–89, https://doi.org/10.1016/j.scriptamat.2018.07.045.
[32] M. Basham, J. Filik, M.T. Wharmby, P.C.Y. Chang, B. El Kassaby, M. Gerring, J. Aishima, K. Levik, B.C.A. Pulford, I. Sikharulidze, D. Sneddon, M. Webber, S. S. Dhesi, F. Maccherozzi, O. Svensson, S. Brockhauser, G. Náray, A.W. Ashton, Data analysis WorkbeNch (DAWN), J. Synchrotron Rad. 22 (2015) 853–858, https://doi.org/10.1107/S1600577515002283.
[33] P. Thompson, D.E. Cox, J.B. Hastings, Rietveld refinement of Debye–Scherrer synchrotron X-ray data from Al_2O_3, J. Appl. Cryst. 20 (1987) 79–83.
[34] D. Balzar, Voigt function model in diffraction-line broadening analysis, in: R. L. Snyder, J. Fiala, H.-J. Bunge (Eds.), Defect and microstructure analysis by diffraction, Repr, Oxford Univ. Press, Oxford, 2005, pp. 94–126.
[35] D. Balzar, N.C. Popa, Analyzing microstructure by Rietveld refinement, Rigaku J. 22 (2005) 16–25.
[36] W.A. Dollase, Correction of intensities for preferred orientation in powder diffractometry: application of the March model, J. Appl. Cryst. 19 (1986) 267–272, https://doi.org/10.1107/s0021889886089458.
[37] V. Petříček, L. Palatinus, J. Plášil, M. Dušek, Jana2020 – a new version of the crystallographic computing system Jana, Z. F. üR. Krist. Cryst. Mater. 238 (2023) 271–282, https://doi.org/10.1515/zkri-2023-0005.
[38] M. Järvinen, Application of symmetrized harmonics expansion to correction of the preferred orientation effect, J. Appl. Crystallogr 26 (1993) 525–531, https://doi.org/10.1107/s0021889893001219.
[39] H. Muguerra, D. Grebille, F. Bourée, Disordered misfit Ca(2)CoO(3)CoO(2)(1.62) structure revisited via a new intrinsic modulation, Acta Crystallogr. B 64 (2008) 144–153, https://doi.org/10.1107/S0108768108001213.
[40] E.-S. Kim, J.-G. Liang, C. Wang, M.-Y. Cho, J.-M. Oh, N.-Y. Kim, Inter-digital capacitors with aerosol-deposited high-K dielectric layer for highest capacitance value in capacitive super-sensing applications, Sci. Rep. 9 (2019) 680, https://doi.org/10.1038/s41598-018-37416-7.
[41] J. Akedo, Microstructure of ceramic thick film formed by aerosol deposition and its applications to microactuator, Integr. Ferroelectr. 80 (2006) 55–65, https://doi.org/10.1080/10584580600656221.
[42] J. Akedo, M. Lebedev, Powder preparation in aerosol deposition method for lead zirconate titanate thick films, Jpn. J. Appl. Phys. 41 (2002) 6980–6984, https://doi.org/10.1143/JJAP.41.6980.
[43] N.H. Khansur, U. Eckstein, M. Sadl, H. Ursic, K.G. Webber, Fabrication of porous thick films using room temperature aerosol deposition, J. Am. Ceram. Soc. 103 (2019), https://doi.org/10.1111/jace.16772.
[44] I.-S. Kim, P.-J. Ko, M.-Y. Cho, Y.-S. Lee, H. Sohn, C. Park, W.H. Shin, S.-M. Koo, D.-W. Lee, J.-M. Oh, Fabrication of high-quality alumina coating through novel, dual-particle aerosol deposition, Ceram. Int. 46 (2020), https://doi.org/10.1016/j.ceramint.2020.06.142.
[45] J. Kim, H. Kwon, H. Park, C. Lee, Microstructural features affecting optical properties of vacuum kinetic sprayed Al_2O_3 thin film, Surf. Interfaces 9 (2017) 114–123, https://doi.org/10.1016/j.surfin.2017.08.007.
[46] Z. Yang, S. Rahmati, A. Dolatabadi, T.W. Coyle, Understanding the effect of surface topography on the formation of aerosol-deposited coatings, Ceram. Int. 51 (2025), https://doi.org/10.1016/j.ceramint.2025.01.431.
[47] G.G. Stoney, The tension of metallic films deposited by electrolysis, Proc. R. Soc. Lond. A 82 (1909) 172–175, https://doi.org/10.1098/rspa.1909.0021.
[48] A. Mézin, Coating internal stress measurement through the curvature method: a geometry-based criterion delimiting the relevance of Stoney's formula, Surf. Coat. Technol. 200 (2006) 5259–5267, https://doi.org/10.1016/j.surfcoat.2005.06.018.
[49] D.G. Isaak, J.D. Carnes, O.L. Anderson, H. Cynn, E. Hake, Elasticity of TiO 2 rutile to 1800 K, Phys. Chem. Miner. 26 (1998) 31–43, https://doi.org/10.1007/s002690050158.
[50] S. Kuroyanagi, K. Shinoda, A. Yumoto, J. Akedo, Size-dependent quasi brittle-ductile transition of single crystalline alpha-alumina particles during microcompression tests, Acta Mater. 195 (2020) 588–596, https://doi.org/10.1016/j.actamat.2020.05.065.
[51] D.-W. Lee, H.-J. Kim, Y.-H. Kim, Y.-H. Yun, S.-M. Nam, Growth process of α-Al2O3 ceramic films on metal substrates fabricated at room temperature by aerosol deposition, J. Am. Ceram. Soc. 94 (2011) 3131–3138, https://doi.org/10.1111/j.1551-2916.2011.04493.x.
[52] K. Naoe, K. Sato, M. Nishiki, Effect of process for producing Al2O3 particles on deposition efficiency in aerosol deposition method, J. Ceram. Soc. Jpn. 122 (2014) 110–116, https://doi.org/10.2109/jcersj2.122.110.
[53] D. Hanft, J. Exner, R. Moos, Thick-films of garnet-type lithium ion conductor prepared by the Aerosol Deposition Method: The role of morphology and annealing treatment on the ionic conductivity, J. Power Sources 361 (2017) 61–69, https://doi.org/10.1016/j.jpowsour.2017.06.061.
[54] J. Henon, M.A. Piechowiak, O. Durand-Panteix, G. Etchegoyen, O. Masson, C. Dublanche-Tixier, P. Marchet, B. Lucas, F. Rossignol, Dense and highly textured coatings obtained by aerosol deposition method from Ti_3SiC_2 powder: comparison to a dense material sintered by Spark Plasma Sintering, J. Eur. Ceram. Soc. 35 (2015) 1179–1189, https://doi.org/10.1016/j.jeurceramsoc.2014.10.012.
[55] M. Suzuki, T. Tsuchiya, J. Akedo, Effect of starting powder morphology on film texture for bismuth layer-structured ferroelectrics prepared by aerosol deposition method, Jpn. J. Appl. Phys. 56 (2017) 06GH02, https://doi.org/10.7567/JJAP.56.06GH02.
[56] R. Werner, J.S. Matejka, D. Schönauer-Kamin, R. Moos, From thermoelectric powder directly to thermoelectric generators: flexible Bi_2Te_3 films on polymer sheets prepared by the powder aerosol deposition method at room temperature, Energy Tech. 10 (2022) 2101091, https://doi.org/10.1002/ente.202101091.
[57] M. Schubert, M. Hahn, J. Exner, J. Kita, R. Moos, Effect of substrate hardness and surface roughness on the film formation of aerosol-deposited ceramic films, Funct. Mater. Lett. 10 (2017) 1750045, https://doi.org/10.1142/S179360471750045X.